HHS Public Access

Opposing Functions of Interferon Coordinate Adaptive and Innate Immune Responses to Cancer Immune Checkpoint Blockade

Joseph L. Benci[1,7,8,*,†], **Lexus R. Johnson**[1,8,*], **Ruth Choa**[4], **Yuanming Xu**[1,8], **Jingya Qiu**[1,8], **Zilu Zhou**[9], **Bihui Xu**[1,8], **Darwin Ye**[1,8], **Katherine L. Nathanson**[2,6], **Carl H. June**[4,6,7,8], **E. John Wherry**[3,5,6,7], **Nancy R. Zhang**[9], **Hemant Ishwaran**[10], **Matthew D. Hellmann**[11,12,14], **Jedd D. Wolchok**[11,12,13,14], **Taku Kambayashi**[4,6], **Andy J. Minn**[1,6,7,8]

[1]Department of Radiation Oncology, Perelman School of Medicine, University of Pennsylvania, Philadelphia, PA 19104, USA

[2]Department of Medicine, Perelman School of Medicine, University of Pennsylvania, Philadelphia, PA 19104, USA

[3]Department of Microbiology, Perelman School of Medicine, University of Pennsylvania, Philadelphia, PA 19104, USA

[4]Department of Pathology and Laboratory Medicine, Perelman School of Medicine, University of Pennsylvania, Philadelphia, PA 19104, USA

[5]Department of Systems Pharmacology and Translational Therapeutics; Perelman School of Medicine, University of Pennsylvania, Philadelphia, PA 19104, USA

[6]Institute for Immunology, Perelman School of Medicine, University of Pennsylvania, Philadelphia, PA 19104, USA

[7]Parker Institute for Cancer Immunotherapy, Perelman School of Medicine, University of Pennsylvania, Philadelphia, PA 19104, USA

[8]Abramson Family Cancer Research Institute, Perelman School of Medicine, University of Pennsylvania, Philadelphia, PA 19104, USA

[9]Department of Statistics, The Wharton School, University of Pennsylvania, Philadelphia, PA 19104, USA

Correspondence to (Lead Contact): Andy J. Minn, MD, PhD, 421 Curie Blvd, BRB II/III, Room 510, Philadelphia, PA 19104, Tel: 215-736-5515, andyminn@upenn.edu.
†Current address: Bristol-Myers Squibb, Princeton, NJ 08540, USA

[10]Division of Biostatistics, Department of Epidemiology and Public Health, University of Miami, Miami, FL 33136, USA

[11]Department of Medicine, Memorial Sloan Kettering Cancer Center, New York, NY 10065, USA

[12]Parker Institute for Cancer Immunotherapy, Memorial Sloan Kettering Cancer Center, New York, NY 10065, USA

[13]Ludwig Collaborative Laboratory, Memorial Sloan Kettering Cancer Center, New York, NY 10065, USA

[14]Department of Medicine, Weill Cornell Medical College, New York, NY 10065, USA

SUMMARY

Interferon-gamma (IFNG) augments immune function yet promotes T cell exhaustion through PDL1. How these opposing effects are integrated to impact immune checkpoint blockade (ICB) is unclear. We show that while inhibiting tumor IFNG signaling decreases interferon-stimulated genes (ISGs) in cancer cells, it increases ISGs in immune cells by enhancing IFNG produced by exhausted T cells (T_{EX}). In tumors with favorable antigenicity, these T_{EX} mediate rejection. In tumors with neoantigen or MHC-I loss, T_{EX} instead utilize IFNG to drive maturation of innate immune cells, including a PD1$^+$TRAIL$^+$ ILC1 population. By disabling an inhibitory circuit impacting PD1 and TRAIL, blocking tumor IFNG signaling promotes innate immune killing. Thus, interferon signaling in cancer cells and immune cells oppose each other to establish a regulatory relationship that limits both adaptive and innate immune killing. In melanoma and lung cancer patients, perturbation of this relationship is associated with ICB response independent of tumor mutational burden.

Graphical Abstract:
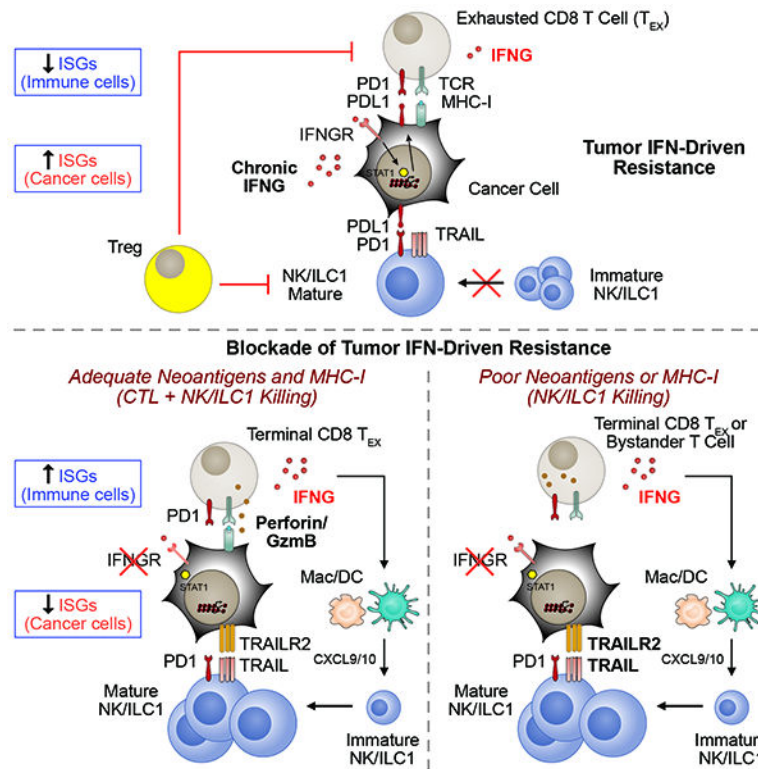
Abstract

The opposing effects of interferon-gamma in terms of regulating immune function but also driving T cell exhaustion through PDL1 is explained by its differential effects in tumor and immune cell populations.

INTRODUCTION

Immune checkpoint blockade (ICB) of the inhibitory receptors CTLA4 and PD1 can result in durable responses in multiple cancer types (Ribas and Wolchok, 2018). Resistance and relapse are common and can be influenced by factors inherent to immune cells, cancer cells, or both (Patel and Minn, 2018). Important immune features include the status of T cell infiltration and the differentiation or activation state of T cells and innate immune cells. Features intrinsic to cancer cells that can impact ICB outcome include their repertoire of neoantigens, the ability to present antigens on major histocompatibility complex class one (MHC-I), and the expression of inhibitory receptor ligands. The clinical relevance of these immune and cancer cell factors is highlighted by common biomarkers for ICB response such as type I or II interferon (IFN) stimulated genes (ISGs) (Ayers et al., 2017; Harlin et al., 2009), tumor mutational burden (TMB) (Rizvi et al., 2015; Snyder et al., 2014), and expression of PDL1 (Taube et al., 2012; Tumeh et al., 2014).

Both IFN-gamma (IFNG) and type I IFN (IFN-I) are among the known pathways that have critical roles in anti-tumor immunity. IFN enhances immune function by inducing expression of MHC-I (Dighe et al., 1994), which is constitutively expressed on many tissues including

cancer cells, and by enabling dendritic cells (DCs) to cross prime T cells (Diamond et al., 2011; Fuertes et al., 2011). In this way, IFNs are important in the early phase of antigen recognition and the interaction between adaptive and innate immune cells. Accordingly, loss-of-function mutations and genomic alterations in the IFN signaling pathway have been associated with clinical ICB resistance and/or relapse (Gao et al., 2016; Shin et al., 2017; Zaretsky et al., 2016), and unbiased genetic screens have identified this same pathway as being important for immunotherapy response in certain mouse models (Manguso et al., 2017; Mezzadra et al., 2017). In contrast, some patients have tumors with mutations in the IFN pathway that nonetheless respond to ICB (Hellmann et al., 2018; Sade-Feldman et al., 2017) or have high serum levels of IFNG that associates with ICB progression (Huang et al., 2017). These apparently "paradoxical" observations may represent feedback inhibition properties of IFN signaling (Snell et al., 2017). In the context of chronic pathogen infection, persistent IFN signaling and ISGs dampen immune responses to prevent immune-mediated pathology while allowing for a host-pathogen stalemate (Cheng et al., 2017; Teijaro et al., 2013; Wilson et al., 2013). In cancer, this dichotomous function of IFN is exploited through chronic signaling by tumor cells that can promote resistance to ICB (Benci et al., 2016). IFN-driven resistance can be inhibited by genetic ablation of the IFNG receptor (IFNGR) and/or IFN-I receptor (IFNAR) in cancer cells, resulting in a decrease in PDL1, other inhibitory ligands, and the GzmB antagonist SERPINB9 (Jiang et al., 2018). Expansion of exhausted T cells (T_{EX}) can then ensue to restore ICB response through unknown mechanisms. Together, these observations highlight the importance of understanding how the opposing functions of IFN signaling impact cancer immunotherapy.

Loss of the beta-2 microglobulin (B2M) subunit of MHC-I appears to be a common resistance mechanism to ICB (Sade-Feldman et al., 2017). However, diminished expression or loss of B2M can also occur in patients who respond to ICB (Rizvi et al., 2018; Rodig et al., 2018), suggesting that innate immune cells might contribute to ICB response in some cases. Indeed, conventional NK cells and innate lymphoid cells (ILCs) are capable of destroying cancers through either perforin-mediated cytotoxicity or TNF-family death receptors such as TRAIL (Spits et al., 2016). NK/ILC effector function is regulated through cellular maturation, combinations of activating and inhibitory receptors, and possibly immune checkpoint receptors like PD-1, TIM3, and TIGIT (Gao et al., 2017; Zhang et al., 2018). Recent evidence indicates that type one ILCs (ILC1s) can participate in anti-tumor immunity or cancer immune surveillance. This includes ILC1-like populations (Dadi et al., 2016) and intratumoral ILC1s that are generally poorly cytotoxic (Cortez et al., 2017; Gao et al., 2017). Although the ability of NK/ILC1s to eradicate tumors with diminished MHC-I and/or a poor neoantigens is of significant interest, how to mobilize these innate immune cells to facilitate tumor response is unclear.

RESULTS

ISGs expressed by cancer cells predict resistance to immune checkpoint blockade while ISGs expressed by immune cells predict response

A large proportion of human cancers differentially express a subset of ISGs that can predict resistance to radiation and chemotherapy (Weichselbaum et al., 2008). Coincidentally, this

ISG resistance signature (ISG.RS) is also associated with resistance to ICB, as demonstrated by elevated expression in ICB-resistant melanoma tumors from Res 499 cells (Figure 1A), which were derived from a B16-F10 tumor (Twyman-Saint Victor et al., 2015). In contrast, ISGs can also predict clinical ICB response, especially ISGs typically associated with IFNG signaling (Ayers et al., 2017). To begin reconciling these seemingly disparate observations, we examined the ISG.RS and genes from the IFNG hallmark gene set (IFNG.GS) by dividing them into two non-overlapping subsets (Figure 1B and Table S1) and creating a metagene (the average scaled expression of all genes in the set). The expression of these ISG metagenes was then examined across different cellular populations in human melanomas using previously published single-cell RNA-seq data (Tirosh et al., 2016). This revealed that the IFNG.GS is predominantly expressed by intratumoral immune cells such as T cells, NK cells, and macrophages (Figure 1B and S1A). In contrast, the ISG.RS is predominantly expressed in cancer cells, albeit with variable expression.

To understand the potential consequences of these differences in IFNG.GS and ISG.RS expression patterns, we analyzed bulk RNA-seq data combined from two cohorts of melanoma patients treated with anti-PD1 (Figure 1C) (Hugo et al., 2016; Riaz et al., 2017). As expected, the majority of genes in the IFNG.GS are depressed in the majority of tumors from nonresponders to anti-PD1 (Figure S1B). However, like ICB-resistant murine Res 499 tumors, most ISG.RS genes are enriched in tumors from non-responders (Figure S1B). Consistent with the importance of CD8 T cells in response, tumors with high IFNG.GS but low ISG.RS also have the greatest proportion of CD8 T cells (Figure 1D, top right quadrant) as inferred by CIBERSORT (Newman et al., 2015) (Figure S1C). The higher frequencies of CD8 T cells are accompanied by increased number of activated NK cells (Figure 1D, orange regression line), which also has been associated with clinical ICB response (Riaz et al., 2017). To understand how these immune and interferon-related variables independently contribute to ICB response, we utilized a multivariable logistic regression model. This revealed that while higher IFNG.GS increases the odds ratio for response, ISG.RS independently decreases the likelihood (Figure 1E). The significance of both of these variables are independent of tumor mutational burden (TMB) status, which expectedly correlates with response. In contrast, neither the abundance of CD8 T cells nor NK cells are significant in the model. A random forest model, which does not assume linearity and incorporates interaction effects, revealed that ISG.RS exhibits a higher importance score than either IFNG.GS or TMB (Figure S1D). In total, these data suggest that while expression of IFNG.GS by immune cells is associated with CD8 T cell abundance, accumulation of activated NK cells, and ICB response, all of these effects are opposed by high levels of ISG.RS in cancer cells.

Although the IFNG.GS and ISG.RS predict opposite clinical outcomes, their expression is positively correlated, consistent with IFN controlling both metagenes (Figure 1F). An explanation for this apparent "paradox" lies in the relative expression of each metagene. When expression of the ISG.RS exceeds the IFNG.GS, resistance is favored (Figure 1F, left plot, red circles below diagonal). In contrast, most responses occur when IFNG.GS is similar to or greater than ISG.RS (Figure 1F, blue circles). Based on these findings, we combined the two metagenes into a ratio of IFNG.GS over ISG.RS (or, the difference of these two metagenes in log transformed space). By logistic regression, this composite variable (dISG)

is strongly associated with response and is independent of TMB (Figure 1F, right plot and inset). Specifically, the probability of response is low when either the ratio or TMB is low but increases when either increase. Furthermore, random forest machine learning and bootstrapping revealed that the ISG ratio has the highest robustness and average variable importance compared to TMB and multiple immune features (Figure S1E).

In total, the single-cell and bulk RNA-seq analysis suggests that distinct ISGs differentially expressed by cancer and immune cells can oppose each other to influence CD8 T cell infiltrate and NK activation, and can be combined into a ratio that predicts ICB response independent of TMB (Figure 1G). Motivated by these findings, we sought to understand the mechanistic underpinnings inferred by these statistical relationships.

Models differing in MHC-I, TMB, and neoantigen status for examining the effect of blocking tumor IFN signaling on ICB response

If the probability of ICB response is influenced by the ratio of IFNG-related ISGs expressed by immune cells over inhibitory ISGs expressed by cancer cells, one way to enhance the ratio in favor of response is to prevent IFN signaling in cancer cells. We first confirmed whether the ISG.RS, which is elevated in ICB-resistant Res 499 tumors, is regulated by IFN signaling in cancer cells (hereafter referred to as tumor IFN signaling). Indeed, CRISPR knockout of IFNGR and/or IFNAR significantly diminishes ISG.RS levels (Figure 1H). However, loss of tumor IFN signaling can render cancers less responsive to immunotherapy due to compromised MHC-I and antigen processing (Manguso et al., 2017; Zaretsky et al., 2016), suggesting that the impact from ablating tumor IFN signaling might be context dependent. In light of this, we surmised two situations whereby the benefit of inhibiting IFN-driven resistance could outweigh the potential negative impact on MHC-I. The first is when constitutive MHC-I is high, minimizing effects that loss of IFN-inducible MHC-I has on CTL-mediated killing. A second situation is when tumors have depleted or poor neoantigens. Here, diminished CTL recognition presumably makes MHC-I status less consequential for T cell-mediating killing, but interference with IFN-driven resistance might improve killing by NK or other innate lymphoid cells.

We first characterized various mouse tumor models for differences in MHC-I expression, TMB, and predicted neoantigen status (Figure 2A). Of these, CT26 colorectal cancer has the highest TMB (Figure 2B) and maintains high MHC-I in the absence of IFNG signaling (Figure 2C–D). Similarly, TSA-derived Res 237 breast cancer cells also have high IFNG-independent baseline MHC-I but exhibit lower TMB (Figure 2B–C and S2A). In contrast, B16 and/or Res 499 melanoma have intermediate TMB, low constitutive MHC-I, and relies on IFNG for high MHC-I expression (Figure 2B–D and S2B). Since Res 499 originated from an abscopal B16 tumor that relapsed several weeks after radiation (RT) plus anti-CTLA4 (Twyman-Saint Victor et al., 2015), we surmised that Res 499 may additionally have undergone immunoediting prior to relapse. Recent evidence suggests that neoantigens that have clonal or near-clonal representation are predominantly targeted by the immune system, while neoantigens at low clonal fractions can remain immunologically silent (Gejman et al., 2018; McGranahan et al., 2016). In accord with this notion, there is a significant decrease in the cumulative frequency of predicted high affinity (<100 nM)

neoantigens with clonal (near-heterozygous or greater) frequencies in Res 499 compared to B16 (Figure 2E, leftward shift orange curve). In particular, a cluster of predicted neoantigens (cluster 6, Figure 2F) are present at clonal frequencies in B16 but fall to subclonal or near-zero frequencies in Res 499 tumors (Figure 2F, lower right quadrant). This cluster of neoantigens is predicted to reside in a subpopulation of cells (subclone 3, Figure 2G) that is nearly eliminated in Res 499 compared to B16, consistent with immunoediting. In contrast, the subpopulation with the largest reciprocal increase in Res 499 (subclone 4) is characterized by a mutation cluster (cluster 7) with low clonal frequencies (Figure 2F, lower left quadrant), as expected for resistant subclones. Together, these data define several tumor models that differ in reliance on IFNG for high MHC-I and in predicted neoantigen availability.

Blocking tumor IFN signaling broadly improves ICB response through CD8 T and innate immune cells

We first used the CT26 model to examine whether tumors with high constitutive MHC-I and TMB demonstrate improved response when ISG.RS is decreased by blocking tumor IFN signaling. Remarkably, when IFNGR or both IFNGR and IFNAR are ablated, mice either show markedly slower tumor growth or spontaneous regression that is CD8 T cell dependent (Figure 3A), as determined by antibody-mediated depletion (Figure S3A). The addition of anti-PD1 further improves anti-tumor effects and survival. Both spontaneous regression and durable response to anti-PD1 requires B2M and hence MHC-I. All mice with complete response are also resistant to tumor rechallenge (8 out of 8 mice), further indicative of a T cell dominant response. Thus, decreasing ISG.RS by preventing IFN signaling in tumors with high baseline MHC-I does not interfere with CTL-mediating killing and markedly enhances immunogenicity.

Unlike CT26, B16 cells are reliant on IFN for high MHC-I expression (Figure S2B). B16 tumors respond poorly to anti-PD1 but respond to RT + anti-CTLA4, a combination that enhances T cell repertoire diversity and improves response over anti-CTLA4 alone (Twyman-Saint Victor et al., 2015). Surprisingly, knockout of IFNGR and IFNAR in B16 tumors does not negatively impact the efficacy of RT + anti-CTLA4 (Figure 3B, top left plots, red vs. orange), suggesting that other immune-mediated killing mechanisms may compensate for low MHC-I and compromised CTL recognition in this context. Indeed, partial response of IFNGR knockout tumors to RT + anti-CTLA4 is maintained even after B2M is ablated (Figure 3B, top left plots, grey vs. light blue). However, when B2M knockout is accompanied by depletion of NK1.1$^+$ cells (Figure S3A), which are typically conventional NK cells and ILC1s, response is completely eliminated (Figure 3B, left top and bottom plots, grey vs red). In contrast to B16, Res 499 tumors are resistant to RT + anti-CTLA4 and have relative depletion of predicted neoantigens (Figures 2E–G). Despite this, knockout of IFNGR and IFNAR restores Res 499 response to levels at least as high as parental B16 tumors (Figure 3B, right plots). Consistent with loss of neoantigens and reliance on innate immune killing, co-ablation of B2M has no discernible effect while depletion of NK1.1$^+$ cells alone abrogates the benefit from IFNGR + IFNAR knockout (Figure 3B, right top and bottom plots). However, if the requirement for high MHC-I and antigen is bypassed by using a murine chimeric antigen receptor (CAR) T cell against

ectopically expressed human CD19 (Figure S3B), blocking tumor IFN signaling similarly improves response of both B16 and Res 499 tumors (Figure 3C). In the absence of CAR T cells, IFNGR + IFNAR knockout tumors grow similarly to control (Figure S3C). Thus, blocking tumor IFN signaling can impact both CD8 T cell and NK/ILC effector function.

In total, these data suggest that blocking tumor IFN signaling can improve T cell-mediated killing when antigen recognition is not limited by inhibiting IFN function, as in the case of CT26 tumors and use of CAR T cell therapy. In tumors with low MHC-I, preventing tumor IFN signaling may compromise CTL-mediated recognition but anti-tumor effects of NK/ILC1s can compensate to maintain response, as in the case of B16 tumors. In tumors such as Res 499 that are highly resistant and otherwise poorly recognized by T cells, the dispensability of MHC-I allows for restored response through NK/ILC-mediated killing.

Inhibition of tumor IFNG signaling enables CD8 T cells to support NK/ILC-mediated killing

To understand how blocking tumor IFN signaling restores ICB response in resistant or relapsed tumors and to avoid conflating effects of type I and II IFN, we focused on how IFNGR knockout restores response in the Res 499 model. We also opted to use anti-CTLA4 monotherapy given that addition of RT does not significantly improve response over anti-CTLA4 alone (Figure 3D vs. 3B). As expected for NK/ILC-mediating killing, IFNGR knockout improves response to anti-CTLA4 in the absence of B2M (Figure 3D and S3D). This requires NK1.1$^+$ innate immune cells (Figure 3D and S3A), is perforin-independent (Figure 3E), and does not generate durable immunity against tumor rechallenge of mice with complete response (Figure S3E). To test if NK/ILC-mediated cytotoxicity may be responsible for response after IFNGR knockout, we co-cultured poly I:C stimulated splenic NK cells with Res 499 cells in vitro (Figure S3F). This resulted in NK-mediated cytotoxicity as measured by CD107a, which is used as a general marker for NK effector function (Ahlenstiel et al., 2010). IFNG treatment of wild type but not IFNGR knockout Res 499 cells prior to co-culture was sufficient to increase resistance even in the absence of B2M, consistent with tumor IFNG signaling impeding NK/ILC killing. Thus, like with inhibition of both type I and II IFN signaling, blocking tumor IFNG signaling can restore ICB response by enhancing NK/ILC-mediated effector function.

Surprisingly, although depletion of NK1.1$^+$ cells abrogates ICB response of IFNGR knockout Res 499 tumors, depletion of CD8 T cells, but not CD4 T cells, also inhibits response (Figure 3D and S3G). A similar requirement for both CD8 T cells and NK/ILC1s is also observed after IFNGR knockout in the resistant TSA/237 breast cancer model that exhibits relatively low TMB and a paucity of predicted strong neoantigens (Figure 2B and S3H). These observations suggest that although CD8 T cells do not directly kill IFNGR knockout Res 499 tumors, they may have a supportive role.

Preventing tumor IFNG signaling enhances immune cell IFNG signaling, CD8 T$_{EX}$ function, and maturation of NK/ILC1 cells

To examine how CD8 T cells might support NK/ILC1s, we employed single-cell RNA-sequencing (scRNA-seq) and 28-color flow cytometry. Analysis of intratumoral CD45$^+$ immune cells by scRNA-seq revealed that a dominant effect of tumor IFNGR knockout is an

increase in the proportion of CD8 T cells (Figure 4A). Intratumoral CD8 T cells are typically exhausted and reside in either a progenitor exhausted or terminally exhausted population (Miller et al., 2019). Although terminally exhausted PD1+ CD8 T cells have limited long-term proliferative potential, they can carry out various effector functions such as cytotoxicity and IFNG production (Miller et al., 2019; Paley et al., 2012). Gene set enrichment analysis (GSEA) using transcriptional signatures of these exhausted subsets (defined using the LCMV infection model) revealed that the expanded CD8 T cells resulting from IFNGR knockout show a marked increase in terminal exhaustion genes (e.g., *Pdcd1*, *Eomes*, *Cd38*) and a decrease in progenitor exhaustion genes (e.g., *Tcf7*) (Figure 4B and S4A). Accordingly, there is a per cell increase in the amount of IFNG protein produced by PD1+ CD8 T cells (Figure S4B), and after anti-CTLA4 there is a large increase in IFNG per gram of tumor (Figure 4C), which is not but observed with cytokines such as IL-6 (Figure S4C). Depletion of CD8 T cells largely abrogates this intratumoral increase in IFNG, highlighting the importance of exhausted CD8 T cells in generating this cytokine. Accompanying the increase in IFNG is a marked increase in the IFNG.GS primarily from myeloid/DC populations (Figure 4D). Among various IFNG.GS genes that increase include *Cxcl9* and *Cxcl10* (Figure 4E), which are chemokines implicated in NK cell recruitment, activation, or maturation (Pak-Wittel et al., 2013). Thus, disrupting tumor IFNG signaling not only decreases the ISG.RS in cancer cells but also increases production of IFNG by terminally exhausted CD8 T cells. As an apparent consequence, myeloid/DC populations increase expression of IFNG.GS that include chemokines important in innate immune function.

In order to investigate how preventing IFNG signaling in tumor cells impacts NK/ILC1 status, we re-clustered NK/ILC1 populations identified by scRNA-seq (Figure 4F–G). This revealed NK populations differing in maturity and effector function (Chiossone et al., 2009), including an immature CD11b^{low} population, an intermediate CD11b^{int} population, and a mature CD11b^{high} cluster that typically possesses the greatest effector function. Moreover, recently described ILC1 and intermediate ILC1 (intILC1) populations (Cortez et al., 2017; Gao et al., 2017) were also identified (Figure S4D). Knockout of tumor IFNGR results in a large shift in the NK populations toward the mature CD11b^{high} cluster and an additional shift toward the ILC1 cluster (Figure 4F, density plots). These ILC1s exhibit relatively high levels of *Pd1* (*Pdcd1*) and *Trail* (*Tfnsf10*) (Figure 4G), consistent with previously reported properties for this population. Using 28-color flow cytometry (Figure S4E–F), we confirmed that tumor IFNGR knockout leads to an increase in the proportion of NK/ILC1s that are CD11b^{high} NK cells or PD1+ TRAIL+ ILC1s (Figure 4H–I and S4G). Flow cytometry also confirmed that this is accompanied by an increase in the proportion of terminally exhausted CD8 T cells, particularly after anti-CTLA4, as indicated by an increase in PD1+ Eomes+ CD8 T cells that express multiple inhibitory receptors and relatively high levels of Ki67 and GzmB (Figure 4H and S4G).

Together, these results indicate that preventing tumor IFNG signaling expands CD8 T$_{EX}$ toward terminal exhaustion and increased production of IFNG. In this way, disrupting tumor IFNGR not only decreases ISG.RS in cancer cells but conversely increases IFNG.GS expression by immune cells. This enhanced IFNG signaling in immune cells might then

drive maturation and function of NK/ILC1 subsets, including a PD1$^+$ TRAIL$^+$ ILC1 population that potentially contributes to ICB response.

Preventing tumor IFNG signaling enables IFNG from CD8 T$_{EX}$ to drive NK/ILC1 function while removing inhibitory feedback from PD1/PDL1 and TRAIL/TRAILR2

Given the single-cell findings, we sought to investigate whether IFNG produced by CD8 T$_{EX}$ is involved in NK/ILC1-mediated killing and whether the PD1/PDL1 and TRAIL/TRAILR pathways, which are implicated due to their presence on intratumoral ILC1s, can contribute to response after IFNGR knockout. To test the role of IFNG produced by CD8 T cells, we adoptively transferred CD8 T cells from wild type or IFNG knockout mice into RAG-deficient hosts and then implanted the mice with Res 499 IFNGR knockout tumors (Figure 5A and S5A). This revealed that IFNG production by CD8 T cells is required for anti-CTLA4 response. Conversely, when CD8 T cells are depleted, there is a decrease in the proportion of mature CD11b$^+$ NK/ILC1s (Figure S5B) as well as total NK/ILC1s (Figure 5B). However, direct intratumoral injection of IFNG or CXCL10 can rescue or partially rescue the loss in NK/ILC1 cells (Figure 5B). NK/ILC1-dependent ICB response (Figure 5C, blue boxplots) and survival (Figure S5C) that is also compromised after depleting CD8 T cells is similarly rescued by injection of IFNG. Thus, these results suggest NK/ILC1-dependent response resulting from blocking tumor IFNG signaling relies on IFNG produced by CD8 T$_{EX}$ and on downstream chemokines such as CXCL10.

Although IFNG has a critical role in promoting NK/ILC1 function, it also induces high levels of PDL1 on tumors. Given that PD1 is expressed on ILC1 cells, this suggests that the PD1/PDL1 axis may normally function as an IFNG-directed feedback inhibition mechanism to antagonize innate immune function, similar to its role in regulating T cell responses. If so, removal of this feedback inhibition by IFNGR knockout may contribute to the improved response resulting from blocking tumor IFNG signaling. To examine this, we ectopically expressed PDL1 in PDL1 knockout Res 499 tumors to make PDL1 levels independent of IFNG signaling (Figure S5D). In contrast to wild type or B2M-deficient Res 499 tumors, the ability of IFNGR deletion to improve anti-CTLA4 response is lost when PDL1 levels are fixed (Figure S5E). To remove effects of PD1 from CD8 T cells, we depleted CD8 T cells but restored NK/ILC1 function in IFNGR-deficient Res 499 tumors by intratumoral administration of IFNG (Figure 5C, red boxplots). Consistent with tumor PDL1 inhibiting NK/ILC1 killing, fixing high PDL1 expression despite IFNGR knockout blunted NK/ILC1-dependent ICB response. Conversely, improved anti-CTLA4 response resulting from PDL1 deletion requires NK/ILC1s (Figure 5D). The notion that PD1/PDL1 can directly inhibit NK/ILC1 killing was also corroborated by using CD49a$^+$ PD1$^+$ liver NK cells cultured with IFNGR-deficient Res 499 cells with and without ectopic PDL1 (Figure 5E and S5F). In total, these results suggest that tumor IFNG signaling normally drives feedback inhibition through tumor PDL1 to regulate NK/ILC1 function. Thus, ablating tumor IFNGR not only increases immune cell IFNG signaling but also enhances innate immune killing by interfering with the PD1/PDL1 inhibitory axis.

Besides PD1, intratumoral ILC1 cells also expresses TRAIL. Since response from tumor IFNGR knockout is independent of host perforin (Figure 3E), this suggests that tumor

killing may utilize the TRAIL/TRAILR pathway. Indeed, Res 499 tumors not only express PDL1 but also the TRAIL receptor (TRAILR2). Unlike PDL1, TRAILR2 decreases in direct response to IFNG in vitro (Figure S5G). Accordingly, knockout of tumor IFNGR significantly increases TRAILR2 in vivo, while PDL1 decreases (Figure 5F). Deletion of TRAILR2 in IFNGR-deficient Res 499 tumors (Figure S5H) reveals that tumor killing after anti-CTLA4 is largely dependent on TRAIL/TRAILR2 interaction (Figure 5G). These data suggest that IFNG controls an inhibitory feedback mechanism for NK/ILC1s not only by increasing tumor PDL1 but also by decreasing TRAILR2. Thus, preventing tumor IFNG signaling enables TRAIL- and NK/ILC1-dependent killing.

Adaptive immune cell requirements for innate immune killing after blocking tumor IFNG signaling

Despite our findings that response after IFNGR knockout of Res 499 tumors requires IFNG produced by CD8 T cells, the dispensability of tumor MHC-I argues that antigen presentation by tumor cells is not necessary for CD8 T_{EX} to support NK/ILC1 function. To corroborate this, we implanted Res 499 tumors deficient in both IFNGR and B2M in either wild type mice or OT-1 mice expressing a transgenic T cell receptor to OVA antigen, which is not expressed by Res 499 tumors (Figure 6A). The accumulation of both intratumoral CD8 T cells and NK/ILC1s is reduced and ICB response is lost in OT-1 mice compared to wild type mice (Figure 6B). However, intratumoral injection of OVA peptide rescued the compromised CD8 T cell frequency and partially restored NK/ILC1 levels. Moreover, despite the absence of tumor MHC-I, response to anti-CTLA4 was also partially rescued (Figure 6C). Thus, the ability of IFNGR knockout to enhance NK/ILC1-dependent ICB response need not depend on antigen presentation by tumor cells themselves. Rather, cross-primed and/or activated bystander T cells can suffice.

Although disrupting tumor IFNG signaling interferes with the inhibitory effects of PD1/PDL1 between tumor cells and both adaptive and innate immune cells, anti-CTLA4 appears to provide a non-redundant function to PD1/PDL1 inhibition. In mouse models, and possibly in humans, antagonistic CTLA4 antibodies not only block CTLA4 but can also deplete CD4^{+} T regulatory cells (Tregs) (Arce Vargas et al., 2018; Romano et al., 2015; Simpson et al., 2013). Indeed, Tregs are among the most proliferative immune cells in Res 499 tumors and this does not appear altered by tumor IFNGR knockout (Figure 6D). To investigate the importance of inhibiting Tregs, we used the 4F10 antibody against CTLA4 that does not concurrently deplete Tregs (Simpson et al., 2013). In contrast to the Treg-depleting 9H10 antibody, 4F10 fails to elicit a response against Res 499 IFNGR knockout tumors (Figure S6A). Conversely, depleting Tregs by stimulation of the diptheria toxin receptor under control of Foxp3 recapitulates the effects of 9H10 on IFNGR-deficient Res 499 tumors (Figure 6E). The non-redundant effect of a Treg-depleting antibody with tumor IFNGR knockout is also highlighted in the CT26 tumor model. Here, although IFNGR knockout results in complete responses to anti-PD1, all mice relapse when B2M is ablated (Figure 6F and S6B). However, the 9H10 anti-CTLA4 antibody results in complete response despite B2M loss, consistent with the anti-CTLA4 but not anti-PD1 antibody allowing for more optimal NK/ILC1-mediated killing. Corroborating the potential role of Tregs in suppressing innate immune cell activity, abundance of activated NK cells inversely associates with Treg

abundance in melanoma patients (Figure 6G). Thus, interfering with the suppressive effects of Tregs may be required to fully unleash both adaptive and innate immune killing resulting from blocking tumor IFNG signaling. These findings imply that dual therapy with anti-PD1 plus anti-CTLA4 antibodies that inhibit Tregs may promote innate immune function better than monotherapy approaches.

Tumor mutations in IFN pathway genes predict clinical response to dual blockade of PD1 and CTLA4

Our findings suggest that mutations predicted to reduce tumor IFN signaling might associate with decreased ISG.RS and improved clinical response to ICB. To investigate this, we extended the analysis of recently described exome-sequencing data of non-small cell lung cancer (NSCLC) patients from either TCGA or a clinical trial using anti-PD1 plus anti-CTLA4 (Hellmann et al., 2018). After excluding common non-disease single-nucleotide variants, pathogenic missense and nonsense mutations were predicted using two algorithms, CADD and DANN, that were trained on a catalog of benign and pathogenic variants from the ClinVar database (Figure S7A; see Methods). Indels were also evaluated as damaging or neutral using SIFT. In the TCGA, there is an 8.6% incidence of patient tumors with at least one predicted pathogenic variant in a core set of 11 type I and II IFN pathway genes (Figure S7B–C). These tumors exhibit a decrease in ISG.RS genes, consistent with an enrichment for IFN pathway variants with defective signaling (Figure 7A and S7D). In the patients treated with anti-PD1 plus anti-CTLA4, 14.7% of patients have at least one IFN pathway variant and these patients have improved progression-free survival (PFS) with dual ICB (Figure 7B–C). In contrast, only 0.58% of random gene sets of similar size yield PFS differences that are as significant (Figure S7E), and IFN pathway variants do not associate with survival in TCGA patients (Figure S7F), arguing that variant status is not a general prognostic marker. Although the presence of IFN pathway variants is associated with higher TMB (Figure S7G), multivariable logistic regression and random forest reveal that variant status predicts ICB response independently of TMB and PDL1 expression (Figure 7D and S7H). Both models yield predicted probabilities of response (CR or PR) that correlate well to actual observed responses (Figure 7E, top panel; Figure S7H, right plot). Notably, despite a higher likelihood of response, variant-positive tumors exhibit lower percent tumor PDL1 expression (5.4% versus 20.3%; Figure 7F), consistent with variants having a negative impact on tumor IFN signaling. In contrast, stratification by variant status of random genes rarely yields a difference in %PDL1 this large (frequency 5.7×10^{-3}) (Figure S7I). Notably, one patient had a tumor with multiple alleles of B2M with a frameshift indel or predicted pathogenic missense mutations who nonetheless had a PR to ICB (Figure 7E, patient 40). This is consistent with previous reports describing a NSCLC patient responding to anti-PD1 despite deleterious B2M mutations and loss of B2M expression confirmed by immunohistochemistry (Rizvi et al., 2018). Thus, genetic alterations of the IFN pathway in human NSCLC are associated with decreased ISG.RS, decreased tumor PDL1, and improved ICB response independent of TMB status.

DISCUSSION

In this study, we describe how IFNG signaling in tumor cells antagonizes both T cell and innate immune responses. This is accomplished through an inhibitory feedback circuit orchestrated by tumor cells whereby IFNG from immune cells not only regulates its own inhibition but tightly controls adaptive and innate immunity (Figure 7G). Our current and previous findings suggest several main components to this IFNG circuit. First, we previously reported that persistent IFNG signaling can initiate epigenetic changes in cancer cells characterized by enhanced STAT1-associated open chromatin (Benci et al., 2016) that includes loci for ISGs belonging to ISG.RS genes (unpublished data). Since resistance caused by persistent IFNG signaling can take several weeks to establish, these results suggest that the first component of the feedback circuit is the establishment of an epigenetic landscape in cancer cells that is permissive for enhanced ISG.RS expression. The second component is enforcing T cell exhaustion through high levels of PDL1 and likely other inhibitory ligands, which may include HVEM, LGALS9, and others (Benci et al., 2016). How the increase in these inhibitory ligands are mechanistically related to the epigenetic changes is currently unclear. Nonetheless, the end result is interactions between cancer and immune cells that favor an exhausted T cell state characterized by decreased IFNG and CTL function. The third component is inhibition of innate immunity by impeding NK/ILC1 effector function and differentiation. IFNG signaling in cancer cells not only increases PDL1 but decreases TRAILR2, which is the receptor for TRAIL expressed by ILC1 cells. Consequently, cytotoxicity from PD1$^+$ TRAIL$^+$ NK/ILC1 cells is antagonized. Additionally, the decreased production of IFNG by T cells further safeguards against innate immune killing by stalling NK/ILC1 recruitment and/or maturation. This may be at least partly due to diminished expression of CXCL9/10 from myeloid cells. Thus, IFNG signaling in cancer cells orchestrates feedback inhibition on multiple levels to limit both adaptive and innate immune function.

By preventing tumor IFNG signaling, both adaptive and innate immune functions are unleashed (Figure 7G). However, the degree to which each of these effector arms contribute to response is context dependent. In tumors that are less reliant on IFNG for high MHC-I expression and antigen presentation (e.g., CT26 and TSA), blocking tumor IFNG signaling enables T$_{EX}$ to coordinate both CTL- and NK/ILC1-mediated responses. For tumors with low baseline MHC-I that are reliant on IFNG to elevate MHC-I expression (e.g., B16), a decrement in CTL killing is likely; however, the presence of innate immune killing can help to maintain overall response. For tumors such as Res 499 with poor neoantigens and low MHC-I, or for tumors that have lost B2M, compromised IFN-inducible MHC-I is likely inconsequential. Here, enhanced IFNG production by cross-primed T$_{EX}$ or possibly activated bystander T cells increases IFNG signaling in immune cells and maturation of NK/ILC1s. Ablating tumor IFNG signaling may particularly help activate otherwise poorly cytotoxic PD1$^+$ TRAIL$^+$ ILC1 cells (Cortez et al., 2017; Gao et al., 2017) by increasing tumor TRAILR2, decreasing PDL1, and/or altering other inhibitory pathways present on NK cells and/or ILC1s (Figure 4G). Thus, preventing tumor IFNG signaling enhances both adaptive and innate immune effector function but the magnitude that each contributes to

response is context-dependent – in particular, MHC status and antigen availability are likely key determinants.

Besides cell-intrinsic properties that influence the extent to which adaptive and innate immunity contribute to response after tumor IFNGR knockout, another important determinant is the impact of therapy on Tregs. In our mouse models, intratumoral Tregs are highly proliferative, consistent with recent evidence from human tumors (Li et al., 2019). Preventing tumor IFNG signaling does not appear to impact the abundance or proliferative status of Tregs. Yet, inhibiting Tregs seems to be an important requirement to fully enable ICB response after tumor IFNGR knockout, particularly response driven by innate immune cells. This may explain why response can be worse when IFNG signaling is crippled in B16 models using anti-PD1-based combination therapies (Manguso et al., 2017). Here, therapeutic efficacy is likely CTL-dominant and IFNG is needed to increase low baseline MHC-I levels. Primarily relying on enhanced CTL killing through PD1 blockade becomes inadequate because MHC-I levels are insufficient for T cell recognition, and NK/ILC1 killing is not effective without concurrently inhibiting Tregs. This notion is illustrated using CT26 tumors that have high baseline MHC-I and is responsive to both anti-PD1 and anti-CTLA4. Here, durable response of IFNGR knockout CT26 tumors to anti-PD1 is abrogated by B2M loss but maintained when using a Treg-depleting anti-CTLA4 antibody. This interpretation may explain why mutations in the IFNG signaling pathway can associate with relapse to anti-PD1 monotherapy if baseline MHC-I levels are inadequate (Zaretsky et al., 2016). In such instances, inhibiting Tregs might promote tumor response through NK/ILC1-mediated killing. Such non-redundant effects between anti-PD1 and potential Treg targeting antibodies may provide insight into why MHC-I levels appear not to correlate with clinical response in patients treated with combination nivolumab and ipilimumab (Rodig et al., 2018). Notably, our cohort of lung cancer patients that show IFN pathway variants can predict improved survival was treated with nivolumab and ipilimumab.

Even if CD8 T cells are not able to effectively mediate direct cytolytic tumor killing, the ability of T_{EX} to generate IFNG is important to promote NK/ILC1 function. Preventing tumor IFNG signaling both enhances CD8 T cell abundance and drives them toward terminal exhaustion, a state characterized by high IFNG production compared to progenitor T_{EX}. Our studies also suggest that IFNG produced by cross-primed and/or activated bystander T cells might be sufficient to sustain NK/ILC1 maturation and NK/ILC1-dependent tumor killing. These findings have relevance for bystander T cells to common viruses and other non-tumor antigens that not only are abundant in human tumors (Simoni et al., 2018) but can be leveraged for immunotherapy (Rosato et al., 2019). One reason why antigen-restriction may not be required is because the stimulatory effects of IFNG on NK/ILC1s are indirect. IFNG from CD8 T cells appear to increase IFNG.GS expression predominantly in DC and myeloid cells, and IFNG.GS genes such as *Cxcl10* then influences intratumoral NK/ILC1 abundance. In melanoma patients, IFNG.GS is also highest in macrophages (Figures 1B and S1A) and positively correlates with the proportion of activated intratumoral NK cells (Figure 6G). Thus, tumor-specific T_{EX} or activated bystander T cells can enhance innate immune responses against cancer when tumor IFNG signaling is blocked.

Besides tumor IFNG signaling, inhibiting IFN-I signaling in tumor cells also diminishes the expression of resistance-associated ISGs and in some cases result in greater anti-tumor responses than IFNGR knockout alone (Benci et al., 2016). Thus, how IFN-I contributes to IFN-driven resistance and differs from IFNG requires additional investigation, as do the roles of individual ISGs in ICB resistance.

STAR METHODS

LEAD CONTACT AND MATERIALS AVAILABILITY

Further information and requests for reagents may be directed to, and will be fulfilled by, the Lead Contact Andy Minn (andyminn@upenn.edu). This study did not generate new unique reagents except for cell lines described below.

EXPERIMENTAL MODEL AND SUBJECT DETAILS

Mice—All animal experiments were performed according to protocols approved by the Institutional Animal Care and Use Committee of the University of Pennsylvania. Five to seven week old female C57BL/6 (stock# 027) and BALB/c (stock# 28) were obtained from Charles River Laboratory. Five to seven week old female C57BL/6 (stock# 000664), Perforin knockout (C57BL/6-Prf1^{tm1Sdz}/J; stock# 002407), IFNG knockout (B6.129SJ-Ifng^{tm1Ts}/J; stock # 002287), RAG1 knockout (B6.129S7-Rag1^{tm1Mom}/J; stock# 002216), OT1 (C57BL/6-Tg(TcraTcrb)1100Mjb/J; stock# 003831), FoxP3-DTR (B6.129(Cg)-Foxp3$^{tm3(DTR/GFP)Ayr}$/J; stock# 016958) were ordered from Jackson Laboratory (Bar Harbor, ME). Mice were maintained under specific pathogen free conditions and randomly assigned to each experimental group.

Cell Lines—B16-F10 melanoma cells (male C57BL/6 mouse), TSA breast cancer cells (female BALB/c mouse), and resistant sublines were derived and cultured as previously described (Twyman-Saint Victor et al., 2015). CT26 colorectal cancer cell lines (female BALB/c mouse) were purchased from ATCC and similarly cultured.

METHOD DETAILS

CRISPR gene targeting—Gene targeting by CRISPR/Cas9 was accomplished by co-transfection of a Cas9 plasmid (Addgene, 41815), the guide sequence (selected using ZiFit Targeter) cloned into the gBlock plasmid, and a plasmid with the puromycin selection marker. Successful targeting of the gene(s) of interest was determined by treating cells with and without 100 ng/mL of IFNG (PeproTech), 1000 units/mL IFN-beta (PBL Assay Science), or both depending on the target gene, and examining PDL1, B2M, or TRAILR2 surface expression by flow cytometry. Knockout cells were sorted from a bulk knockout population using Fluorescence Activated Cell Sorting (FACS) on the Aria (BD) or FACSJazz (BD) to maintain the diversity of the parent cells. The gene block contains 20 bp target size (N), U6 promoter, gRNA scaffold, and a termination signal. The common gene block sequence is:

TGTACAAAAAAGCAGGCTTTAAAGGAACCAATTCAGTCGACTGGATCCGGTACCA
AGGTCGGGCAGGAAGAGGGCCTATTTCCCATGATTCCTTCATATTTGCATATACGAT

ACAAGGCTGTTAGAGAGATAATTAGAATTAATTTGACTGTAAACACAAAGATATTA
GTACAAAATACGTGACGTAGAAAGTAATAATTTCTTGGGTAGTTTGCAGTTTTAAA
ATTATGTTTTAAAATGGACTATCATATGCTTACCGTAACTTGAAAGTATTTCGATTTC
TTGGCTTTATATATCTTGTGGAAAGGACGAAACACCG**NNNNNNNNNNNNNNNNNNNN
NN**GTTTTAGAGCTAGAAATAGCAAGTTAAAATAAGGCTAGTCCGTTATCAACTTGA
AAAAGTGGCACCGAGTCGGTGCTTTTTTTCTAGACCCAGCTTTCTTGTACAAAGTT
GGCATTA

The guide sequences used are previously published (Benci et al., 2016) or listed in the Key Resources Table.

***In vivo* mouse studies—**Tumor injection and treatment schedule were done as previously described (Twyman-Saint Victor et al., 2015). Except for some experiments to measure immune cell infiltration, both flanks were implanted. Blocking antibodies were given on days 5, 8, and 11 unless otherwise specified. Anti-CD8, anti-NK1.1., and anti-Asialo-GM1 were given on days −2, 0, 4, 8, 12, and 16. Antibodies against CTLA4 (9H10), PDL1 (10F.9G2), or PD1 (RMP1–14) were all administered intraperitoneally at 200 ug/dose. Isotype controls were used to confirm the lack of non-specific effects and a similar response and survival to untreated mice.

Whole exome sequencing—Genomic DNA was isolated and purified from sorted cancer cells from mouse tumors using Purelink Genomic DNA Kit (Fisher). Exome libraries were prepared using the SureSelectQXT Kit (Agilent) with SureSelectXT Mouse All Exon bait. Libraries were sequenced on an Illumina HiSeq 2500 with 100 base paired end reads.

Single Cell Sequencing Preparation—Tumors were harvested on day 17 and viable CD45$^+$ cells were FACS sorted. Single-cell emulsions were obtained using the 10x Genomics Controller and the v2 Library and Gel Bead kit (10X Genomics). RNA-sequencing libraries were prepared as instructed by the 10× 3' v2 kit protocol. Resulting libraries were sequenced on an Illumina NextSeq using a NextSeq 500/550 v2.5 High Output Kit.

Flow cytometry—Tumors were harvested at day 13–15 post tumor implantation. Single-cell suspensions were prepared and red blood cells were lysed using ACK Lysis Buffer (Life Technologies). For in vitro cell lines, untreated or sub-confluent cells treated for 16 hours with 100 ng/mL of IFNG (PeproTech) were harvested and single-cell suspensions prepared. Live/dead cell discrimination was performed using Live/Dead Fixable Aqua Dead Cell Stain Kit (Life Technologies). Cell surface staining was done for 30 min at 4 degrees. Intracellular staining was done using a fixation/permeabilization kit (eBioscience). Data acquisition was done using an LSR II (BD) or FACSCalibur (BD) and analysis was performed using FlowJo (TreeStar) or the *flowCore* package in the R language and environment for statistical computing. For high-dimensional flow cytometry, a FACSymphony (BD) was used for data acquisition and data analysis was done using the *cytofkit* R package and a custom analysis pipeline described in Quantification and Statistical Analysis. For quantitation of immune infiltration, tumors were harvested and weighed and the entire tumor section was dissociated and stained. All events were collected on a flow cytometer and the total number of events of

a given immune cell type were divided by the weight of the tumor. The antibodies used in flow cytometry are provided in the Key Resources Table.

Intratumoral cytokine assay—Approximately 200 ug of tumor was harvested, weighed, and placed in complete RPMI media for 4 hours at 37 degrees. The media was then harvested, spun to remove any remaining cells, and analyzed for cytokine expression (Luminex) according to the manufacturer's instructions. Resulting cytokine levels were then divided by the initial tumor weight for each sample.

In vivo cytokine rescue studies—All mice were pre-treated with anti-CD8 two days before tumor injection. Either 1 ug IFNG or 100 ng CXCL10 was mixed in the PBS/tumor cell suspension prior to injection of the tumor. Mice then continued receiving 500–1000 ng IFNG or 100 ng CXCL10 intra/peritumorally every 3 days post-tumor implantation. For flow cytometry experiments, mice were harvested at day 13 to examine the effects of cytokine addback on immune recruitment in the absence of CD8 T cells. For survival experiments, intra/peritumoral injections continued every 3 days for the remainder of the experiment.

OT1 and FoxP3-DTR mice studies—Transgenic OT1 mice or littermate wild type mice were implanted with tumors using Res 499 cells with IFNGR and B2M knockout. Groups receiving Ova peptide had 50 ng of peptide mixed into the suspension prior to tumor injection and continued to receive intra/peritumoral injections on days 3, 6, 9, and 12. For flow cytometry experiments, mice were harvested on day 13. For FoxP3-DTR mice studies, mice were implanted with Res 499 IFNGR knockout tumors and diptheria toxin was administered intraperitonally at 1 ug/dose/mouse on days 5, 8, and 11 post-injection.

Murine chimeric antigen receptor T cells—B16-F10 or Res 499 tumor cells were transduced with pCLPs-hCD19 lentivirus to express a truncated human CD19 antigen that is unable to drive intracellular signaling. Cells were double sorted for stable expression. 5×10^4 tumor cells in log phase growth were implanted into flanks of B6 mice. Murine T cells were stimulated with CD3/CD28 Dynabeads (Invitrogen) for 24 hours and then transduced with pMSGV-h19BBz retrovirus. At 48 hours after transduction, CAR-expressing T cells were quantified and 5×10^6 CAR-expressing T cells were injected i.v. in mice bearing B16- or Res499-hCD19 tumors 5 days after tumor implantation. Controls were either mock PBS-injected or control transduced CAR T cells, which gave comparable results.

Adoptive transfer of mouse T cells—T cells from spleens of wild type or IFNG knockout mice were isolated by negative selection, and 8×10^6 cells were adoptively transferred i.v. into RAG1$^{-/-}$ mice. Recipient mice were allowed to reconstitute for 4 weeks, verified for reconstitution, and then were injected with flank tumors and treated with ICB as described above.

In vitro NK cell assays—Mice were injected i.p. with poly I:C 18 hours prior to NK cell isolation from mouse spleens or livers by negative selection. NK cells were then cultured with tumor cells for 6 hours. Flow cytometry was performed to assess the effector function and activation status of NK cells by examining CD49a, CD49b, PD1, and/or CD107a.

QUANTIFICATION AND STATISTICAL ANALYSIS

Analysis of tumor growth, survival, and group differences—Tumor volumes were determined by caliper measurements. Differences in survival were determined for each group by the Kaplan-Meier method and the overall p-value was calculated by the log-rank test using the *survival* R package. For mouse studies, an event was defined as death or when tumor burden reached a pre-specified size to minimize morbidity. Using the *MASS* R package, a mixed effect generalized linear model with lognormal distribution for tumor volume data was used to determine differences in growth curves. The significance of all two-way comparisons was determined by a two-sample two-tailed t-test, or by a one-tailed t-test when appropriate. For non-parametric data, a Wilcoxon rank-sum test was used.

Gene set enrichment analysis—RNA-sequencing data from Res 499 resistant cells and B16-F10 parental cells flow sorted from untreated tumor-bearing mice were used for gene expression analysis. Previously described upregulated ISGs associated with cancer and therapy resistance (Weichselbaum et al., 2008) were confirmed to be enriched in Res 499 compared to B16 by gene set enrichment analysis (GSEA) and denoted the ISG Resistance Signature (ISG.RS). For genes associated with IFNG signaling, the IFNG gene set from the Hallmark gene sets was used (IFNG.GS). GSEA was performed and the normalized enrichment scores and p-values calculated using the *fgsea* R package. For some genes like OAS1, orthologs were used when converting between mouse and human gene names. See Table S1 for a list of genes in the ISG.RS and IFNG.GS.

Analysis of genomic features from clinical melanoma samples—Processed bulk RNA-seq data from two different cohorts of melanoma patients treated with anti-PD1 (Hugo et al., 2016; Riaz et al., 2017) were downloaded from the GEO. CIBERSORT (Newman et al., 2015) was used to infer relative frequencies of immune cells in the tumor. For immune cell types with values for both resting and activated states, the values for the resting state were subtracted from values for the activated state. To calculate metagenes, gene expression data were centered and scaled using the sample mean and standard deviation, respectively. Then, the average expression of the genes in each gene set was calculated for each sample to give the metagene value. For tumor mutational burden, the provided values were log10 transformed.

Single-cell RNA-sequencing analysis—Single-cell RNA-sequencing data from melanoma patients were downloaded from the GEO (Tirosh et al., 2016) and converted to TPM values. Several filtering steps were performed including, eliminating genes with low average expression and genes with greater than 20% zero values. This resulted in 8213 genes that was then imputed using the *SAVER* R package (Huang et al., 2018) followed by log2 transformation. Dimensionality reduction was performed using tSNE as implemented in the *Rtsne* R package and resulting clusters were annotated using the provided cell type labels. The expression of each ISG metagene for cells belonging to each cell type was calculated and compared by two sample t-test. For single-cell immune cell data from mouse tumors using the 10X Genomics platform, data were first processed using the *Cell Ranger* pipeline (10X Genomics). This included demultiplexing BCL files into FASTQ, performing alignment with STAR, UMI counting, and aggregating replicates of the same condition.

Cells that had fewer than 500 genes detected, over 10% mitochondrial content, or over 3.5 times the median UMI count were removed. Genes expressed in less than 1% of cells were also removed. After these QC steps, UMI counts were imputed with *SAVER*. *Seurat* was then used to normalize data to sequencing depth using a LogNormalize implementation, and mitochondrial contamination and cell cycle effects were regressed out. Clustering was performed using *Seurat's* graph-based clustering approach and visualized with tSNE. Clusters were classified using a collection of manually curated immune marker genes (Table S2). Metagene values for IFNG.GS was determined similarly to the clinical analysis. The average scaled values for *Mki67* and *Top2a*, and the average scaled values for *Cxcl9* and *Cxcl10* were used to calculate the proliferation and Cxcl9/10 metagene, respectively. For visualization purposes, metagene values less than or greater than 2.5 times the interquartile range were removed. Comparison of expression values between groups was done using a Wilcoxon rank-sum test. GSEA was performed using the *fgsea* R package. Gene sets for LCMV terminal exhausted T cells, progenitor exhausted T cells, and intratumoral ILC1 populations were curated from previously published reports (Gao et al., 2017; Miller et al., 2019).

Multivariable classification, regression, and survival analysis—Random forest (RF) for classification, regression, and survival analysis is a multivariable non-parametric ensemble partitioning tree method that can be used to model the effect of all interactions between genes on a response variable (Breiman, 2001; Chen and Ishwaran, 2012). We used the *randomForestSRC* package version 2.5.1.14 and the following parameters: 5000 trees, node size of 2, and default values for mtry. The default splitting rule was used for classification and the log-rank slitting rule was used for survival analysis. The default value for nsplit was used except for models containing both two-level factor variables and continuous variables. In this case, the nsplit parameter was set to 2 in order to prevent bias against the factor-level variables. Importance scores were calculated using the random ensemble method. For classification problems where the two classes were imbalanced, a random forest quantileclassifier approach was employed. Response was defined as complete or partial response. All predicted values, error rates, and importance scores were based on cross-validation using out-of-bag samples. For variable selection and assessing variable robustness, we considered the set of immune cell frequencies (inferred by CIBERSORT), TMB, IFNG.GS, ISG.RS, and/or the difference between IFNG.GS and ISG.RS (dISG) in a model for immune checkpoint blockade response. Prior treatment status and cohort were included to ensure the lack of confounding from these variables. Balanced undersampling of the majority class was performed and variable selection was determined using minimal depth (Ishwaran et al., 2010). The frequency that each variable was selected and its associated importance score were averaged over 100 iterations.

To complement the RF approach for modeling probability of clinical response to immune checkpoint blockade, we also performed multivariable logistic regression. From this, odds ratios and 95% confidence intervals were determined for each log10 increase in TMB or 0.5 unit increase in metagene expression values. To complement RF variable selection using minimal depth, we performed lasso regression using the *glmnet* R package. Both RF and linear regression methods yielded comparable results.

High-dimensional flow cytometry analysis—Fluorescence intensity data were analyzed using the *flowCore* R package and transformed using the logicle method. After excluding debris, dead cells, doublets and CD45⁻ cells, CD8 T cells and NK/ILC1 cells were gated and separately analyzed. CD8 T cells were identified as TCRB⁺ and CD8⁺, while NK/ILC1 cells were identified as TCRB⁻ and NK1.1⁺. For each population, an aggregate data matrix from random sampling of 1000 events from each sample was used for dimensionality reduction and for clustering analysis. Clusters were identified using Phenograph (Levine et al., 2015) as implemented in the *cytofkit* R package and visualized by tSNE. Using cluster membership as class definitions, a RF classifier was developed using the same aggregate data matrix. After confirming a low misclassification error rate for each class, this RF classifier was used to assign all cells in all samples to one of the clusters. Using the two-dimensional tSNE coordinates, a RF classifier was also developed and used to assign all cells to the tSNE map, allowing the distribution and frequencies of immune cells across clusters to be estimated for each sample. To analyze which immune clusters are strongly associated with wild type or IFNGR knockout tumors, the frequencies of immune cells within each cluster were used as features in a RF model, and the resulting importance scores were examined.

Whole exome sequencing and neoantigen prediction—Preprocessing and variant calling were done with the Genome Analysis Toolkit (GATK) version 4.0.2.1 following its Best Practices workflow. In brief, raw paired-end reads were aligned to the reference mouse genome GRCm38 release 68 using the *bwa-mem* algorithm from BWA version 0.7.17. Duplicates were marked using *MarkDuplicates* from Picard tools version 2.17.11. Systematic errors in base quality scores were detected and recalibrated using GATK's *BaseRecalibrator* and *ApplyBQSR*. Known variants for recalibration were downloaded from the Mouse Genome Project SNP and Indel release version 5. Somatic SNVs and indels were then called with *Strelka* and *MuTect2* using a matched normal germline of either C57BL/6 or BALB/c mice, and only variants shared by both methods were kept. Variants were then filtered with *FilterMutectCalls* using GATK's preset thresholds that are tuned for diploid somatic analyses. Based on gene expression from RNA-seq data, variants from transcripts that were not detectably expressed were removed. The MHC-I binding affinities of variants were then predicted using NetMHC version 4.0 for H-2-Kb and H-2-Db using peptide lengths from 8 to 11. To examine the genomic contraction of variants in Res 499 compared to parental B16, the variant allele frequencies were analyzed for variants with near-heterozygous frequency (0.2 for a tetraploid genome) in one cell line but subclonal frequency in the other. Significance between the distribution of allelic frequencies between the two groups was estimated by a KS-test and compared to 1000 random variants. In addition, subclonal structure and their frequencies within the tumor were examined using the *Canopy* R package (Jiang et al., 2016). High quality variants that meet all the following criteria were used for the analysis: 1) affects only single nucleotides, 2) resides in autosome exonic regions, 3) exhibits VAF variance greater than 0.01, and 4) has mutation calling QUALs that exceed 50. The number of subclones were selected based on a Bayesian information criterion (BIC) after 100000 rounds of simulation across 20 chains. The configuration with the highest posterior likelihood was utilized to generate a phylogenetic tree and the corresponding frequencies of the subclonal populations were determined.

Variant analysis of clinical lung cancer tumors—We used previously published processed data for somatic non-synonymous variants from non-small cell lung cancer patients treated with anti-PD1 and anti-CTLA4 (CheckMate-012 study) or from TCGA (Hellmann et al., 2018). Variants in one of 11 genes involved in type I or II IFN pathway signaling (IFNGR1, IFNGR2, IFNAR1, IFNAR2, JAK1, JAK2, TYK2, STAT1, STAT2, IRF9, and B2M) were examined. To exclude likely normal or benign variants, missense variants were annotated with *ANNOVAR*. Any missense variant found in all individuals in the ExAC database at a relative frequency greater than 0.0001 was removed. In order to predict benign from pathogenic missense or nonsense variants, two algorithms for scoring deleterious variants were used that included DANN, a deep learning algorithm, and CADD, a machine learning algorithm. For each method, an optimal cut point was selected by training on ClinVar data. Here, ClinVar variants classified as likely benign were considered benign and those classified as likely pathogenic were classified as pathogenic. The optimal cut points based on ROC accuracy were then applied to test accuracy in predicting these labels. Any variant below the ROC cut points for both DANN and CADD was categorized as benign. This yielded an overall accuracy of 0.80, sensitivity of 0.95, and specificity of 0.54. This criterion was then applied to the TCGA lung cancer data and the lung cancer tumors from CheckMate-012. For indels, SIFT was used for evaluation and non-frameshift indels and indels predicted to be neutral were excluded. Examining the IFN pathway variants, any patient with at least one predicted pathogenic missense variant, pathogenic nonsense mutation, or deleterious indel resulting in a frameshift was classified as IFN pathway variant positive.

The progression-free survival (PFS) of patients stratified by IFN pathway variant status was determined by Kaplan-Meier survival. The likelihood of response was determined by a multivariable logistic regression using variant status, log10 transformed values for TMB, and a previously used %PDL1 staining cut off of greater than or equal to 1%. The p-value for odds ratios was calculated by bootstrapping. In addition, a non-parametric model for response employing multivariable random forest was also used and without the need to transform any of the variables. The out-of-bag error rate and importance scores from this random forest model was then determined. To evaluate the significance of the observed association between IFN pathway variant status with PFS and decreased %PDL1 staining, the variant status of random sets of 11 genes were evaluated and used to stratify patients. Then, the hazard ratio for PFS and the associated p-value, and the %PDL1 staining for variant-positive and negative patients were recorded for 10,000 iterations and compared to the observed values.

DATA AND CODE AVAILABILITY

All software used in this study are open source and/or publicly available. The datasets generated or used in this study are available at the Gene Expression Omnibus (GEO) at http://www.ncbi.nlm.nih.gov/geo, provided as supplementary data from cited studies, or available through other cited public repositories.

Software—The R language and environment for statistical computing and graphics (https://www.r-project.org) was used for statistical and bioinformatics analysis. R packages

described in methods were obtained from Bioconductor (https://www.bioconductor.org) or from CRAN (https://cran.r-project.org/web/packages/). These packages and additional software for processing, alignment, and analysis of sequencing data are listed in the Key Resources Table.

Data Resources

Mouse sequencing data: The RNA sequencing data for sorted Res 499 tumor cells is available from the GEO under accession number GSE83848. The single-cell RNA sequencing data for immune cells from Res 499 tumors and whole-exome sequencing data from sorted B16 and Res 499 tumors have been deposited under accession number GSE131927.

Human gene expression data: Normalized transcriptomic data, summarized exome analysis, and annotations for human melanoma patients treated with anti-PD1 were previously described (Hugo et al., 2016; Riaz et al., 2017) and downloaded from the GEO under accession number GSE78220 or on GitHub at https://github.com/riazn/bms038_analysis. Single-cell RNA-sequencing data from melanoma patients (Tirosh et al., 2016) were downloaded from the GEO under accession number GSE72056.

Human lung cancer variant data: Processed variant data from non-small cell lung cancer patients treated with anti-PD1 and anti-CTLA4 and from TCGA have been previously described and made available as supplementary information (Hellmann et al., 2018).

ClinVar data: All available data from ClinVar were downloaded from the FTP link available at the website (https://www.ncbi.nlm.nih.gov/clinvar).

Supplementary Material

Refer to Web version on PubMed Central for supplementary material.

ACKNOWLEDGEMENTS

DECLARATION OF INTERESTS

A.J.M. is a project member of the Parker Institute for Cancer Immunotherapy and has received research funding from Merck. He has also received honoraria and travel support from Merck, AstraZeneca, Pfizer, and Takeda. A.J.M. is an inventor on patents related to the IFN pathway, and A.J.M. and L.R.J. are inventors on a filed patent related to modified CAR T cells. J.L.B. is currently an employee of Bristol-Myers Squibb.

E.J.W. is a member of the Parker Institute for Cancer Immunotherapy and has consulting agreements with and/or is on the scientific advisory board for Merck, Roche, Pieris, Elstar, and Surface Oncology. E.J.W. has a patent licensing agreement on the PD-1 pathway with Roche/Genentech and is a founder of Arsenal Biosciences.

REFERENCES

Ahlenstiel G, Titerence RH, Koh C, Edlich B, Feld JJ, Rotman Y, Ghany MG, Hoofnagle JH, Liang TJ, Heller T, et al. (2010). Natural killer cells are polarized toward cytotoxicity in chronic hepatitis C in an interferon-alfa-dependent manner. Gastroenterology 138, 325–35.e1–2. [PubMed: 19747917]

Arce Vargas F, Furness AJS, Litchfield K, Joshi K, Rosenthal R, Ghorani E, Solomon I, Lesko MH, Ruef N, Roddie C, et al. (2018). Fc Effector Function Contributes to the Activity of Human Anti-CTLA-4 Antibodies. Cancer Cell 33, 649–663.e4. [PubMed: 29576375]

Ayers M, Lunceford J, Nebozhyn M, Murphy E, Loboda A, Kaufman DR, Albright A, Cheng JD, Kang SP, Shankaran V, et al. (2017). IFN-γ-related mRNA profile predicts clinical response to PD-1 blockade. J Clin Invest 127, 2930–2940. [PubMed: 28650338]

Benci JL, Xu B, Qiu Y, Wu TJ, Dada H, Twyman-Saint Victor C, Cucolo L, Lee DSM, Pauken KE, Huang AC, et al. (2016). Tumor Interferon Signaling Regulates a Multigenic Resistance Program to Immune Checkpoint Blockade. Cell 167, 1540–1554.e12. [PubMed: 27912061]

Breiman L (2001). Random forests. Machine Learning.

Chen X, and Ishwaran H (2012). Random forests for genomic data analysis. Genomics 99, 323–329. [PubMed: 22546560]

Cheng L, Ma J, Li J, Li D, Li G, Li F, Zhang Q, Yu H, Yasui F, Ye C, et al. (2017). Blocking type I interferon signaling enhances T cell recovery and reduces HIV-1 reservoirs. J Clin Invest 127, 269–279. [PubMed: 27941247]

Chiossone L, Chaix J, Fuseri N, Roth C, Vivier E, and Walzer T (2009). Maturation of mouse NK cells is a 4-stage developmental program. Blood 113, 5488–5496. [PubMed: 19234143]

Cortez VS, Ulland TK, Cervantes-Barragan L, Bando JK, Robinette ML, Wang Q, White AJ, Gilfillan S, Cella M, and Colonna M (2017). SMAD4 impedes the conversion of NK cells into ILC1-like cells by curtailing non-canonical TGF-β signaling. Nat Immunol 122, 91.

Dadi S, Chhangawala S, Whitlock BM, Franklin RA, Luo CT, Oh SA, Toure A, Pritykin Y, Huse M, Leslie CS, et al. (2016). Cancer Immunosurveillance by Tissue-Resident Innate Lymphoid Cells and Innate-like T Cells. Cell 164, 365–377. [PubMed: 26806130]

Diamond MS, Kinder M, Matsushita H, Mashayekhi M, Dunn GP, Archambault JM, Lee H, Arthur CD, White JM, Kalinke U, et al. (2011). Type I interferon is selectively required by dendritic cells for immune rejection of tumors. Journal of Experimental Medicine 208, 1989–2003. [PubMed: 21930769]

Dighe AS, Richards E, Old LJ, and Schreiber RD (1994). Enhanced in vivo growth and resistance to rejection of tumor cells expressing dominant negative IFNγ receptors. Immunity 1, 447–456. [PubMed: 7895156]

Fuertes MB, Kacha AK, Kline J, and Woo SR (2011). Host type I IFN signals are required for antitumor CD8+ T cell responses through CD8α+ dendritic cells. Journal of …

Gao J, Shi LZ, Zhao H, Chen J, Xiong L, He Q, Chen T, Roszik J, Bernatchez C, Woodman SE, et al. (2016). Loss of IFN-γ Pathway Genes in Tumor Cells as a Mechanism of Resistance to Anti-CTLA-4 Therapy. Cell 1–18.

Gao Y, Souza-Fonseca-Guimaraes F, Bald T, Ng SS, Young A, Ngiow SF, Rautela J, Straube J, Waddell N, Blake SJ, et al. (2017). Tumor immunoevasion by the conversion of effector NK cells into type 1 innate lymphoid cells. Nat Immunol 18, 1004–1015. [PubMed: 28759001]

Gejman RS, Chang AY, Jones HF, DiKun K, Hakimi AA, Schietinger A, and Scheinberg DA (2018). Rejection of immunogenic tumor clones is limited by clonal fraction. eLife 7, 635.

Harlin H, Meng Y, Peterson AC, Zha Y, Tretiakova M, Slingluff C, McKee M, and Gajewski TF (2009). Chemokine expression in melanoma metastases associated with CD8+ T-cell recruitment. Cancer Research 69, 3077–3085. [PubMed: 19293190]

Hellmann MD, Nathanson T, Rizvi H, Creelan BC, Sanchez-Vega F, Ahuja A, Ni A, Novik JB, Mangarin LMB, Abu-Akeel M, et al. (2018). Genomic Features of Response to Combination Immunotherapy in Patients with Advanced Non-Small-Cell Lung Cancer. Cancer Cell 33, 843–852.e844. [PubMed: 29657128]

Huang AC, Postow MA, Orlowski RJ, Mick R, Bengsch B, Manne S, Xu W, Harmon S, Giles JR, Wenz B, et al. (2017). T-cell invigoration to tumour burden ratio associated with anti-PD-1 response. Nature 545, 60–65. [PubMed: 28397821]

Huang M, Wang J, Torre E, Dueck H, Shaffer S, Bonasio R, Murray JI, Raj A, Li M, and Zhang NR (2018). SAVER: gene expression recovery for single-cell RNA sequencing. Nat Methods 15, 539–542. [PubMed: 29941873]

Hugo W, Zaretsky JM, Sun L, Song C, Moreno BH, Hu-Lieskovan S, Berent-Maoz B, Pang J, Chmielowski B, Cherry G, et al. (2016). Genomic and Transcriptomic Features of Response to Anti-PD-1 Therapy in Metastatic Melanoma. Cell 165, 35–44. [PubMed: 26997480]

Ishwaran H, Kogalur UB, Gorodeski EZ, Minn AJ, and Lauer MS (2010). High-Dimensional Variable Selection for Survival Data. Journal of the American Statistical Association 105, 205–217.

Jiang P, Gu S, Pan D, Fu J, Sahu A, Hu X, Li Z, Traugh N, Bu X, Li B, et al. (2018). Signatures of T cell dysfunction and exclusion predict cancer immunotherapy response. Nat. Med 24, 1550–1558. [PubMed: 30127393]

Jiang Y, Qiu Y, Minn AJ, and Zhang NR (2016). Assessing intratumor heterogeneity and tracking longitudinal and spatial clonal evolutionary history by next-generation sequencing. Proc Natl Acad Sci USA 113, E5528–E5537. [PubMed: 27573852]

Levine JH, Simonds EF, Bendall SC, Davis KL, Amir E-AD, Tadmor MD, Litvin O, Fienberg HG, Jager A, Zunder ER, et al. (2015). Data-Driven Phenotypic Dissection of AML Reveals Progenitor-like Cells that Correlate with Prognosis. Cell 162, 184–197. [PubMed: 26095251]

Li H, van der Leun AM, Yofe I, Lubling Y, Gelbard-Solodkin D, van Akkooi ACJ, van den Braber M, Rozeman EA, Haanen JBAG, Blank CU, et al. (2019). Dysfunctional CD8 T Cells Form a Proliferative, Dynamically Regulated Compartment within Human Melanoma. Cell 176, 775–789.e18. [PubMed: 30595452]

Manguso RT, Pope HW, Zimmer MD, Brown FD, Yates KB, Miller BC, Collins NB, Bi K, LaFleur MW, Juneja VR, et al. (2017). In vivo CRISPR screening identifies Ptpn2 as a cancer immunotherapy target. Nature Publishing Group 547, 1–17.

McGranahan N, Furness AJS, Rosenthal R, Ramskov S, Lyngaa R, Saini SK, Jamal-Hanjani M, Wilson GA, Birkbak NJ, Hiley CT, et al. (2016). Clonal neoantigens elicit T cell immunoreactivity and sensitivity to immune checkpoint blockade. Science 351, 1463–1469. [PubMed: 26940869]

Mezzadra R, Sun C, Jae LT, Gomez-Eerland R, de Vries E, Wu W, Logtenberg MEW, Slagter M, Rozeman EA, Hofland I, et al. (2017). Identification of CMTM6 and CMTM4 as PD-L1 protein regulators. Nature 549, 106–110. [PubMed: 28813410]

Miller BC, Sen DR, Abosy Al, R., Bi K, Virkud YV, LaFleur MW, Yates KB, Lako A, Felt K, Naik GS, et al. (2019). Subsets of exhausted CD8+ T cells differentially mediate tumor control and respond to checkpoint blockade. Nat Immunol 20, 326–336. [PubMed: 30778252]

Newman AM, Liu CL, Green MR, Gentles AJ, Feng W, Xu Y, Hoang CD, Diehn M, and Alizadeh AA (2015). Robust enumeration of cell subsets from tissue expression profiles. Nat Methods 12, 453–457. [PubMed: 25822800]

Pak-Wittel MA, Yang L, Sojka DK, Rivenbark JG, and Yokoyama WM (2013). Interferon-γ mediates chemokine-dependent recruitment of natural killer cells during viral infection. Proc Natl Acad Sci USA 110, E50–E59. [PubMed: 23248310]

Paley MA, Kroy DC, Odorizzi PM, Johnnidis JB, Dolfi DV, Barnett BE, Bikoff EK, Robertson EJ, Lauer GM, Reiner SL, et al. (2012). Progenitor and terminal subsets of CD8+ T cells cooperate to contain chronic viral infection. Science 338, 1220–1225. [PubMed: 23197535]

Patel SA, and Minn AJ (2018). Combination Cancer Therapy with Immune Checkpoint Blockade: Mechanisms and Strategies. Immunity 48, 417–433. [PubMed: 29562193]

Riaz N, Havel JJ, Makarov V, Desrichard A, Urba WJ, Sims JS, Hodi FS, Martín-Algarra S, Mandal R, Sharfman WH, et al. (2017). Tumor and Microenvironment Evolution during Immunotherapy with Nivolumab. Cell 171, 934–949.e15. [PubMed: 29033130]

Ribas A, and Wolchok JD (2018). Cancer immunotherapy using checkpoint blockade. Science 359, 1350–1355. [PubMed: 29567705]

Rizvi H, Sanchez-Vega F, La K, Chatila W, Jonsson P, Halpenny D, Plodkowski A, Long N, Sauter JL, Rekhtman N, et al. (2018). Molecular Determinants of Response to Anti-Programmed Cell Death (PD)-1 and Anti-Programmed Death-Ligand 1 (PD-L1) Blockade in Patients With Non-Small-Cell Lung Cancer Profiled With Targeted Next-Generation Sequencing. J. Clin. Oncol 36, 633–641. [PubMed: 29337640]

Rizvi NA, Hellmann MD, Snyder A, Kvistborg P, Makarov V, Havel JJ, Lee W, Yuan J, Wong P, Ho TS, et al. (2015). Mutational landscape determines sensitivity to PD-1 blockade in non-small cell lung cancer. Science 348, 124–128. [PubMed: 25765070]

Rodig SJ, Gusenleitner D, Jackson DG, Gjini E, Giobbie-Hurder A, Jin C, Chang H, Lovitch SB, Horak C, Weber JS, et al. (2018). MHC proteins confer differential sensitivity to CTLA-4 and PD-1 blockade in untreated metastatic melanoma. Sci Transl Med 10, eaar3342. [PubMed: 30021886]

Romano E, Kusio-Kobialka M, Foukas PG, Baumgaertner P, Meyer C, Ballabeni P, Michielin O, Weide B, Romero P, and Speiser DE (2015). Ipilimumab-dependent cell-mediated cytotoxicity of regulatory T cells ex vivo by nonclassical monocytes in melanoma patients. Proc Natl Acad Sci USA 112, 6140–6145. [PubMed: 25918390]

Rosato PC, Wijeyesinghe S, Stolley JM, Nelson CE, Davis RL, Manlove LS, Pennell CA, Blazar BR, Chen CC, Geller MA, et al. (2019). Virus-specific memory T cells populate tumors and can be repurposed for tumor immunotherapy. Nat Comms 10, 567.

Sade-Feldman M, Jiao YJ, Chen JH, Rooney MS, Barzily-Rokni M, Eliane J-P, Bjorgaard SL, Hammond MR, Vitzthum H, Blackmon SM, et al. (2017). Resistance to checkpoint blockade therapy through inactivation of antigen presentation. Nat Comms 8, 1136.

Shin DS, Zaretsky JM, Escuin-Ordinas H, Garcia-Diaz A, Hu-Lieskovan S, Kalbasi A, Grasso CS, Hugo W, Sandoval S, Torrejon DY, et al. (2017). Primary Resistance to PD-1 Blockade Mediated by JAK1/2 Mutations. Cancer Discov 7, 188–201. [PubMed: 27903500]

Simoni Y, Becht E, Fehlings M, Loh CY, Koo S-L, Teng KWW, Yeong JPS, Nahar R, Zhang T, Kared H, et al. (2018). Bystander CD8+ T cells are abundant and phenotypically distinct in human tumour infiltrates. Nature 557, 575–579. [PubMed: 29769722]

Simpson TR, Li F, Montalvo-Ortiz W, Sepulveda MA, Bergerhoff K, Arce F, Roddie C, Henry JY, Yagita H, Wolchok JD, et al. (2013). Fc-dependent depletion of tumor-infiltrating regulatory T cells co-defines the efficacy of anti-CTLA-4 therapy against melanoma. Journal of Experimental Medicine 210, 1695–1710. [PubMed: 23897981]

Snell LM, McGaha TL, and Brooks DG (2017). Type I Interferon in Chronic Virus Infection and Cancer. Trends Immunol 38, 542–557. [PubMed: 28579323]

Snyder A, Makarov V, Merghoub T, Yuan J, Zaretsky JM, Desrichard A, Walsh LA, Postow MA, Wong P, Ho TS, et al. (2014). Genetic basis for clinical response to CTLA-4 blockade in melanoma. N Engl J Med 371, 2189–2199. [PubMed: 25409260]

Spits H, Bernink JH, and Lanier L (2016). NK cells and type 1 innate lymphoid cells: partners in host defense. Nat Immunol 17, 758–764. [PubMed: 27328005]

Taube JM, Anders RA, Young GD, Xu H, Sharma R, McMiller TL, Chen S, Klein AP, Pardoll DM, Topalian SL, et al. (2012). Colocalization of inflammatory response with B7-h1 expression in human melanocytic lesions supports an adaptive resistance mechanism of immune escape. Sci Transl Med 4, 127ra37–127ra37.

Teijaro JR, Ng C, Lee AM, Sullivan BM, Sheehan KCF, Welch M, Schreiber RD, Carlos de la Torre J, and Oldstone MBA (2013). Persistent LCMV Infection Is Controlled by Blockade of Type I Interferon Signaling. Science 340, 207–211. [PubMed: 23580529]

Tirosh I, Izar B, Prakadan SM, Wadsworth MH, Treacy D, Trombetta JJ, Rotem A, Rodman C, Lian C, Murphy G, et al. (2016). Dissecting the multicellular ecosystem of metastatic melanoma by single-cell RNA-seq. Science 352, 189–196. [PubMed: 27124452]

Tumeh PC, Harview CL, Yearley JH, Shintaku IP, Taylor EJM, Robert L, Chmielowski B, Spasic M, Henry G, Ciobanu V, et al. (2014). PD-1 blockade induces responses by inhibiting adaptive immune resistance. Nature 515, 568–571. [PubMed: 25428505]

Twyman-Saint Victor C, Rech AJ, Maity A, Rengan R, Pauken KE, Stelekati E, Benci JL, Xu B, Dada H, Odorizzi PM, et al. (2015). Radiation and dual checkpoint blockade activate non-redundant immune mechanisms in cancer. Nature 520, 373–377. [PubMed: 25754329]

Weichselbaum RR, Ishwaran H, Yoon T, Nuyten DSA, Baker SW, Khodarev N, Su AW, Shaikh AY, Roach P, Kreike B, et al. (2008). An interferon-related gene signature for DNA damage resistance is a predictive marker for chemotherapy and radiation for breast cancer. Proc Natl Acad Sci USA 105, 18490–18495. [PubMed: 19001271]

Wilson EB, Yamada DH, Elsaesser H, Herskovitz J, Deng J, Cheng G, Aronow BJ, Karp CL, and Brooks DG (2013). Blockade of Chronic Type I Interferon Signaling to Control Persistent LCMV Infection. Science 340, 202–207. [PubMed: 23580528]

Zaretsky JM, Garcia-Diaz A, Shin DS, Escuin-Ordinas H, Hugo W, Hu-Lieskovan S, Torrejon DY, Abril-Rodriguez G, Sandoval S, Barthly L, et al. (2016). Mutations Associated with Acquired Resistance to PD-1 Blockade in Melanoma. N Engl J Med 375, 819–829. [PubMed: 27433843]

Zhang Q, Bi J, Zheng X, Chen Y, Wang H, Wu W, Wang Z, Wu Q, Peng H, Wei H, et al. (2018). Blockade of the checkpoint receptor TIGIT prevents NK cell exhaustion and elicits potent anti-tumor immunity. Nat Immunol 19, 723–732. [PubMed: 29915296]

HIGHLIGHTS

- Blocking tumor IFNG signaling increases IFNG generated by exhausted T cells (T_{EX})

- Higher immune vs cancer ISGs disable inhibitory pathways, allows NK/ILC1s to mature

- Tumors with adequate MHC-I and antigen are killed by T_{EX} after checkpoint therapy

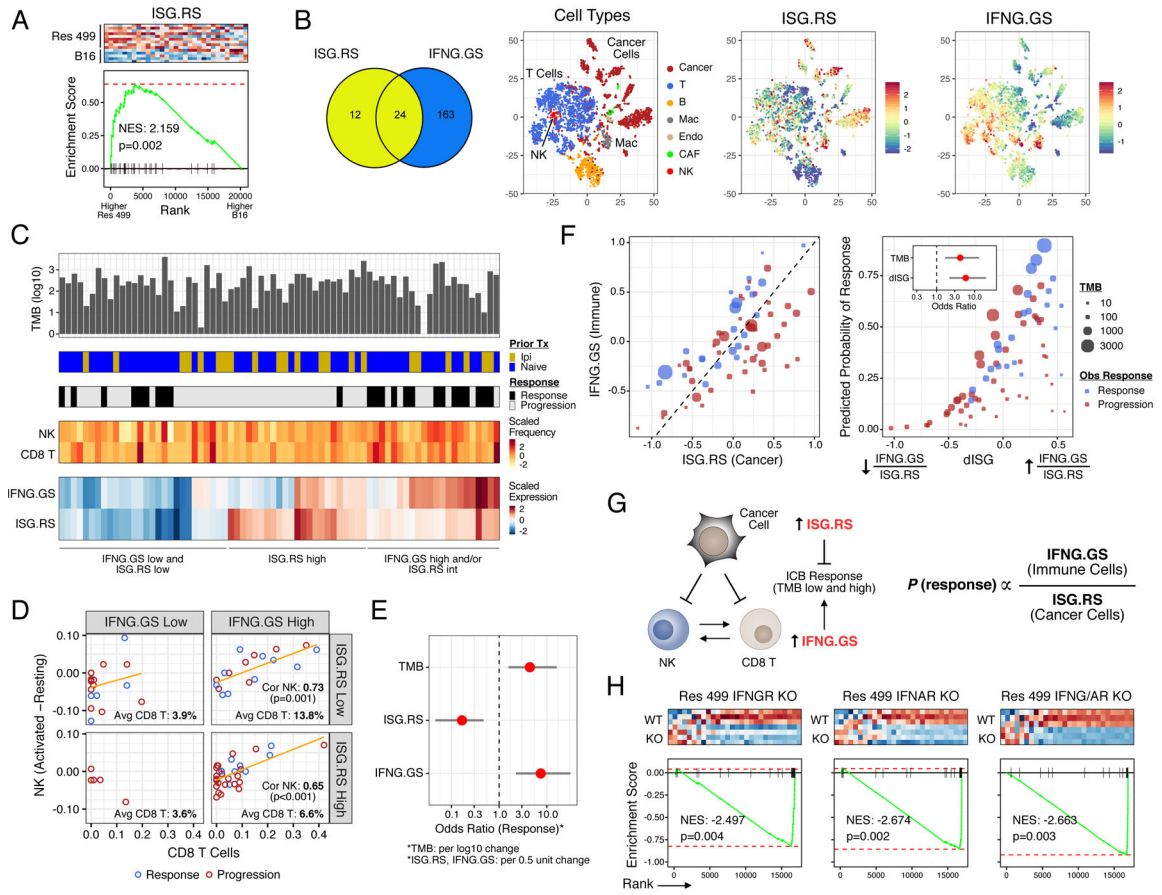- Tumors with low/absent MHC-I or poor antigens are killed by PD1^{+} TRAIL[+] NK/ILC1s

Figure 1. Distinct ISGs are differentially expressed in cancer and immune cells and have opposing functions in predicting clinical ICB response.

A) Gene set enrichment analysis (GSEA) of resistance-associated ISGs (ISG.RS) in Res 499 cells compared to parental B16 cells, both sorted from in vivo tumors. Heatmap (red is high expression, blue is low) and enrichment plot is shown along with the normalized enrichment score (NES) and p-value. **B)** Venn diagram of genes in the ISG.RS along with hallmark IFNG-related genes (IFNG.GS) partitioned into non-overlapping gene sets (color-coded) and used to create individual metagenes. Cell types from scRNA-seq data of pooled human melanoma tumors are shown in the tSNE plot along with expression of the ISG metagenes. **C)** Genomic and clinical features associated with anti-PD1 response in melanoma patients. Shown are tumor mutational burden (TMB), prior treatment with ipilimumab (Ipi), relative frequency of CD8 T cells and activated NK cells (activated minus resting) inferred by CIBERSORT, and bulk tumor expression of the ISG metagenes. **D)** Proportion of activated NK cells vs. CD8 T cells stratified by low/high IFNG.GS and ISG.RS expression. Regression line (orange), Pearson correlation and p-value, and percent CD8 T cells in each quadrant are shown. **E)** Odds ratio and 95% confidence intervals from a multivariable model for clinical anti-PD1 response. **F)** Expression of each metagene (left plot), and the predicted probability of anti-PD1 response (right plot) from a model using TMB and the ratio of IFNG.GS over ISG.RS (dISG). Odds ratios are shown in the inset. Circle color indicates response and size indicates TMB. **G)** Summary of cancer and immune cell relationships inferred by statistical modeling and how ISGs impact probability of ICB response. **H)** GSEA

for ISG.RS genes after KO of the indicated IFN receptor in Res 499 tumors. See also Figure S1.
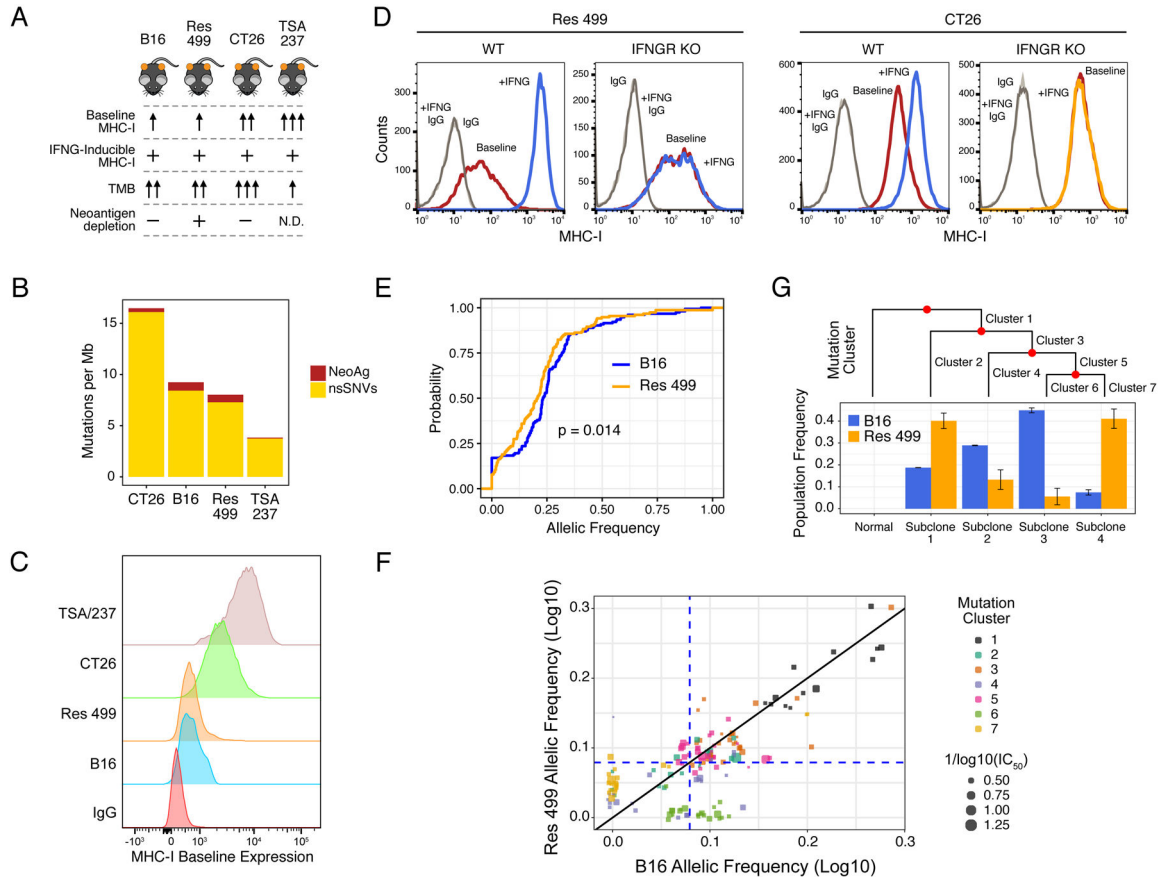
Figure 2. Mouse models differing in MHC-I, tumor mutational burden, and predicted neoantigen status.

A) Summary of key properties of mouse tumor models. N.D. is not determined. **B)** TMB for each of the indicated cell lines. The proportion of predicted neoantigens (MHC-I affinity 500 nM) is shown. **C)** Constitutive (baseline) and **D)** IFNG-inducible (+IFNG) MHC-I on indicated tumor cells with or without IFNGR KO. **E)** Cumulative distribution function plot of the allelic frequencies for predicted high-affinity (100 nM) neoantigens. The p-value is determined by an empirical distribution of the KS statistic from random variants. **F)** Allelic frequency of predicted high-affinity neoantigens in B16 and Res 499 tumors. Values are transformed onto a log10 scale with a near-heterozygous value for a tetraploid genome indicated (dashed blue line). Circle size corresponds to neoantigen affinity. Circle color corresponds to neoantigen clusters predicted to be evolutionarily related and giving rise to **G)** subclonal populations (Subclone 1–4) inferred from high quality variants and displayed using a phylogenetic tree. Frequencies of these subclonal populations are shown. See also Figure S2.
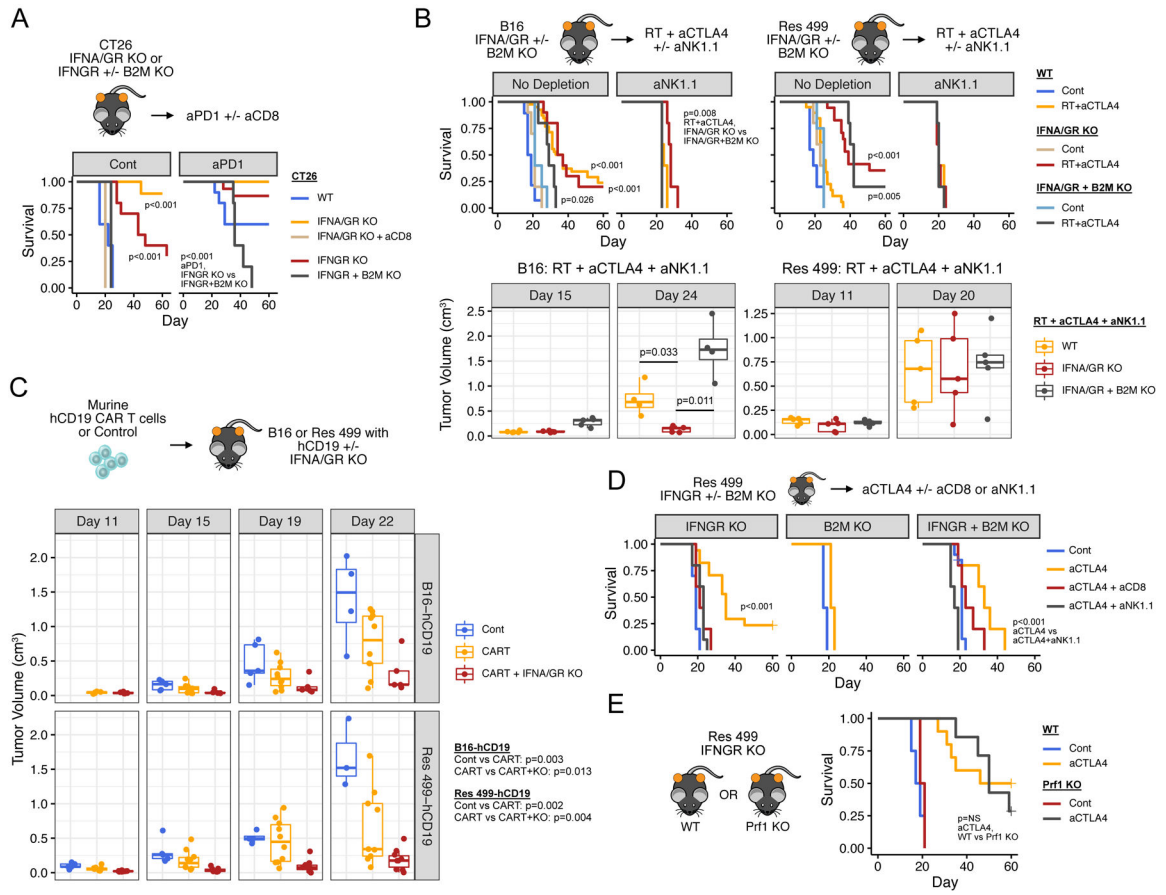
Figure 3. Preventing tumor IFN signaling promotes CD8 T cell-dependent and/or NK/ILC1-dependent ICB response.

A) Survival of mice bearing CT26 tumors with KO of IFNGR +/− B2M or of both IFNGR and IFNAR (IFNA/GR) after no treatment (Cont), CD8 depletion (aCD8), or anti-PD1 (aPD1). For each group, n=5–15. **B)** Survival (top) and tumor volumes (bottom) after treatment with RT + anti-CTLA4 or control (Cont) for mice bearing B16 or Res 499 tumors with the indicated KO. Unless indicated, displayed p-values are for comparisons within each genotype (legend). For tumor volumes, only groups of interest are shown. Groups with no depletion: WT, n=20–28; IFNA/GR KO, n=10–20; IFNA/GR + B2M KO, n=4–5. For aNK1.1 groups, n=5. **C)** Tumor volumes for B16 and Res 499 tumors expressing human CD19 (hCD19) with or without IFNA/GR KO after a single infusion with primary murine T cells transduced with a CAR (CART) against hCD19. **D)** Survival of mice bearing IFNGR KO Res 499 tumors with or without concurrent B2M KO after treatment with anti-CTLA4. Effect of immune cell depletion with anti-CD8 or anti-NK1.1 is shown. IFNGR KO, n=5; B2M KO, n=5; IFNGR + B2M KO, n=10–20. **E)** Survival of wild type (WT) or Perforin KO (Prf1 KO) mice bearing IFNGR KO Res 499 tumors after anti-CTLA4. aCTLA4, n=7–10; Cont, n=2–4. See also Figure S3.
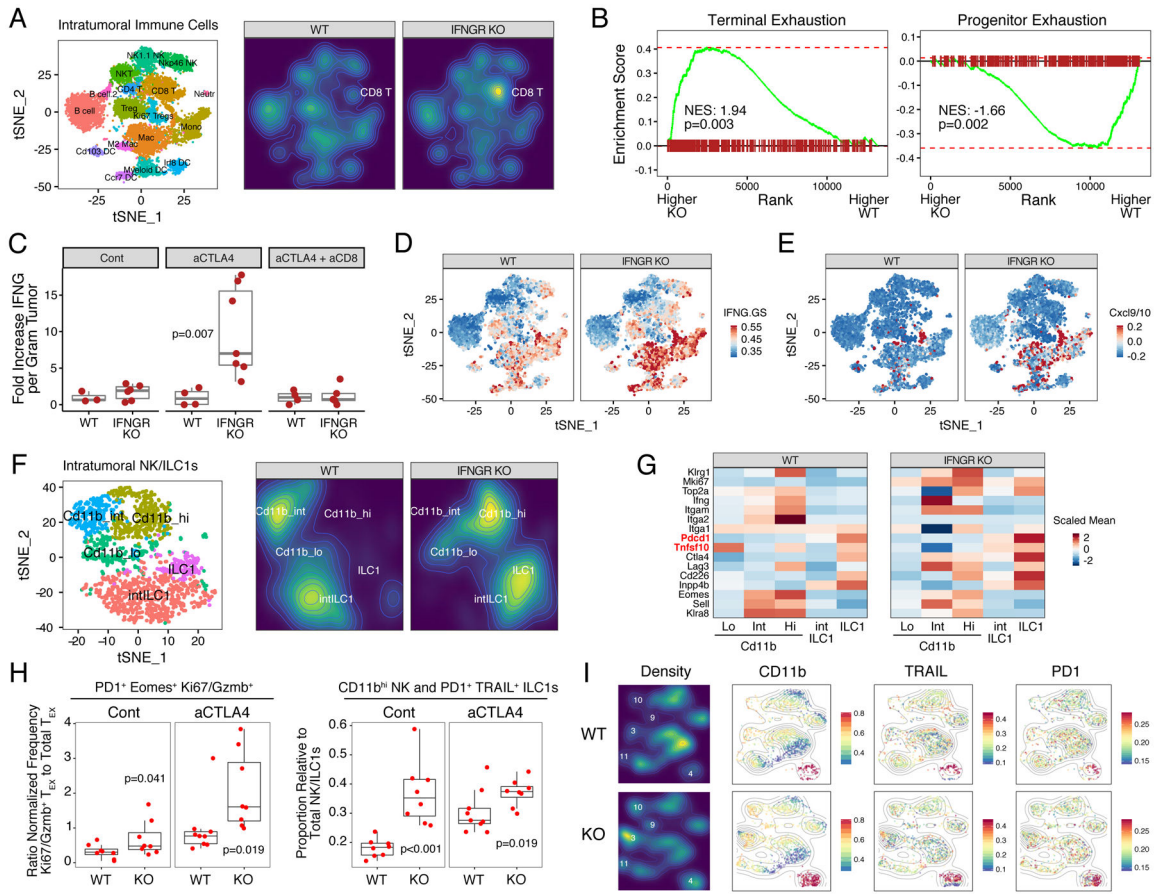
Figure 4. Blockade of tumor IFNG signaling promotes CD8 T$_{EX}$ expansion, IFNG production, immune cell IFNG signaling, and maturation of NK and PD1$^+$ TRAIL$^+$ ILC1 cells.
CD45$^+$ immune cells from Res 499 tumors with or without IFNGR KO were profiled by scRNA-seq. **A)** tSNE plot with identified immune populations (left) and corresponding density plots (right). The percent of CD8 T cells is 6.4% and 16.8% in wild type (WT) and IFNGR KO tumors, respectively. **B)** GSEA on CD8 T cell clusters using T cell terminal exhaustion and progenitor exhaustion gene sets. **C)** Intratumoral IFNG protein levels from wild type or IFNGR KO Res 499 tumors treated with or without anti-CTLA4. Effect of CD8 T cell depletion (aCD8) is also shown. **D)** Expression of IFNG.GS or **E)** average expression of *Cxcl9* and *Cxcl10* across intratumoral immune cells from wildtype or IFNGR KO tumors overlaid on the tSNE map shown in (A). **F)** NK1.1$^+$ and NKp46$^+$ NK cell clusters from (A) were re-clustered. Shown is a tSNE plot with identified NK and ILC1 populations (left) and corresponding density plots (right). **G)** Average expression of select NK/ILC1 genes for each of the indicated NK or ILC1 maturation stage. **H)** CD8 T cells and NK/ILC1 populations were identified by 28-color flow cytometry. Shown is ratio of PD1$^+$ Eomes$^+$ CD8 T$_{EX}$ that belong to Ki67$^+$ GzmB$^+$ clusters over total PD1$^+$ Eomes$^+$ CD8 T$_{EX}$ (left) or the proportion of CD11b^{hi} NK and PD1$^+$ TRAIL$^+$ ILC1 cells relative to total NK/ILC1s (right). **I)** Density plots of NK/ILC1 clusters and expression of indicated markers overlaid onto a tSNE plot. Points are colored by scaled MFI and overlaid with a contour plot. Clusters 3, 9, 10, and 11 are CD11b^{hi} NK cells, and cluster 4 is PD1$^+$ TRAIL$^+$ ILC1 cells. See also Figure S4.
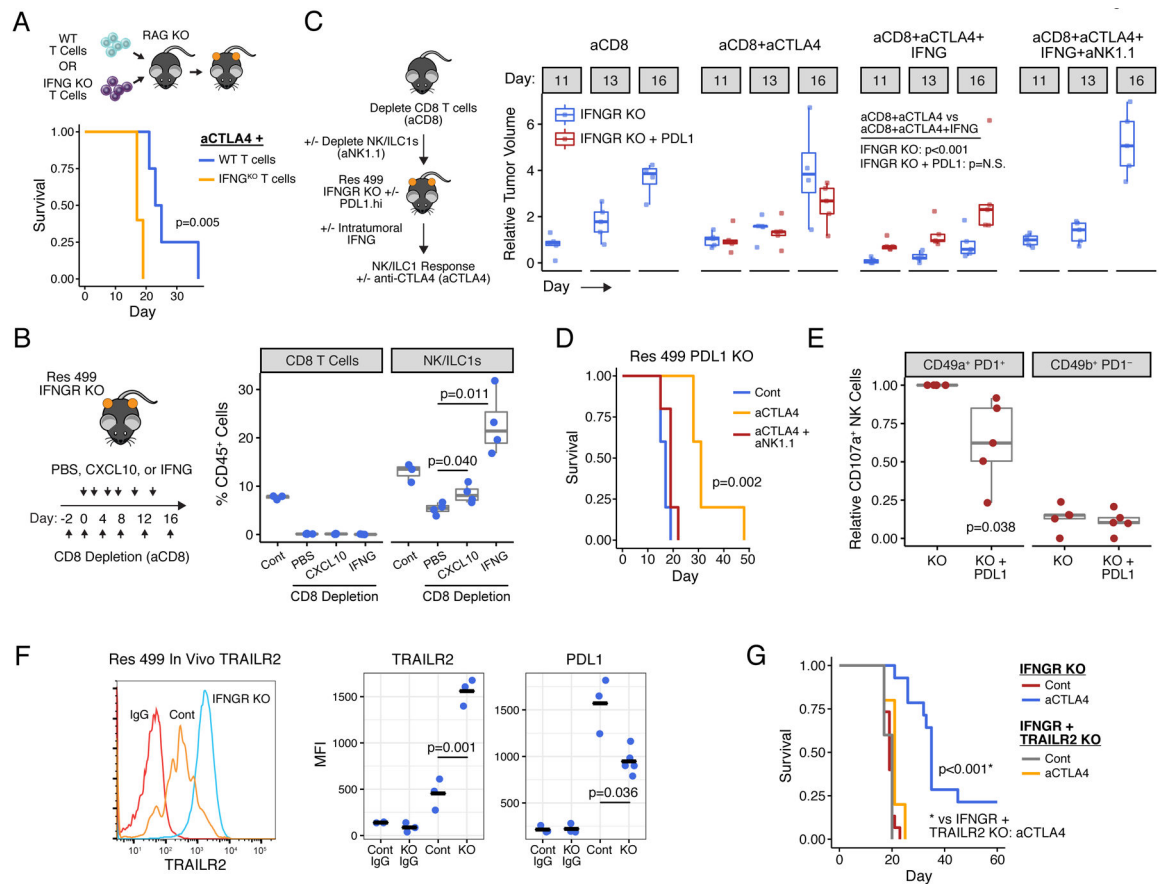
Figure 5. NK/ILC1-mediated killing from blocking tumor IFNG signaling is regulated by IFNG produced by T$_{EX}$, PD1/PDL1, and TRAIL/TRAILR2.
A) Wild type or IFNG-deficient CD8 T cells were adoptively transferred into *Rag1*$^{-/-}$ mice. Shown is survival after implantation of IFNGR KO Res 499 tumors and treatment with anti-CTLA4 (n=4–5). **B)** Mice bearing IFNGR KO Res 499 tumors were depleted of CD8 T cells followed by intratumoral injection of the indicated cytokine. Shown is the percentage of intratumoral CD8 T cells and NK/ILC1s. **C)** Response of IFNGR KO Res 499 tumors in CD8 T cell-depleted mice. Mice were treated with anti-CTLA4 with or without intratumoral injection of IFNG. Effect of concurrent depletion of NK/ILC1s with anti-NK1.1 is also shown as well as effect of high constitutive PDL1 on IFNGR KO tumors (red boxplots). Tumor volumes are relative to initial control tumor volume. **D)** Survival after anti-CTLA4 treatment of mice bearing Res 499 tumors with concurrent KO of PDL1 (n=5). The effect of anti-NK1.1 is shown. **E)** In vitro NK cell killing of Res 499 IFNGR KO tumor cells with or without constitutive ectopic PDL1 expression. Both CD49a$^+$ PD1$^+$ and CD49b$^+$ PD1$^-$ populations were tested. Shown are relative proportions of CD107a$^+$ NK cells. For each biological replicate, data are normalized to results from Res 499 IFNGR KO cells cultured with CD49a$^+$ PD1$^+$ NK cells. **F)** In vivo TRAILR2 and PDL1 expression on Res 499 tumors with or without IFNGR KO. **G)** Survival after anti-CTLA4 of mice bearing IFNGR KO Res 499 tumors with (n=14–15) or without (n=5) concurrent KO of TRAILR2. See also Figure S5.
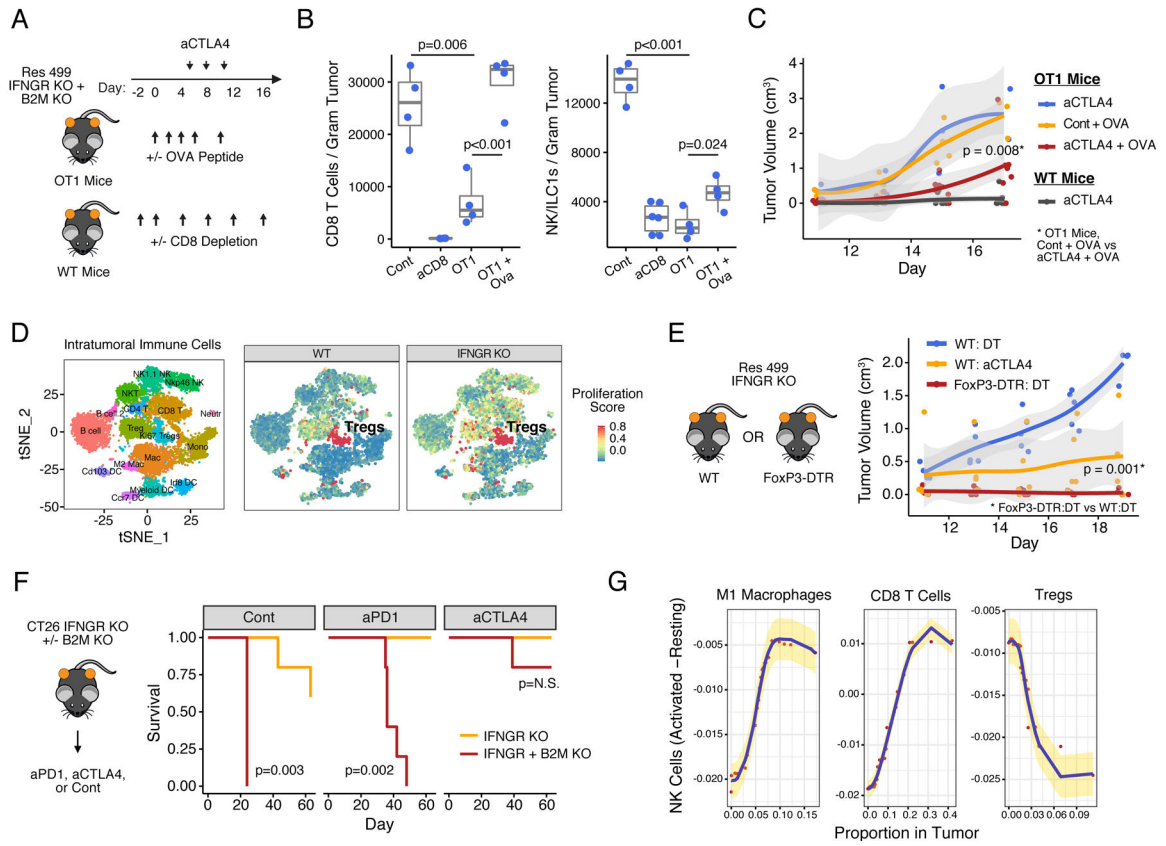
Figure 6. Activated bystander T cells support and Tregs inhibit NK/ILC1-dependent response after blocking tumor IFNG signaling.

A) OT-1 mice bearing Res 499 tumors with combined IFNGR and B2M KO were treated with anti-CTLA4 with or without intratumoral injection of OVA peptide. Wild type mice with or without CD8 T cell depletion were used as comparison. **B)** Tumor infiltration by CD8 T cells and NK/ILC1s and **C)** growth of Res 499 IFNGR + B2M KO tumors after anti-CTLA4 (95% confidence interval in grey). **D)** Proliferation status of Tregs and other intratumoral immune cells in control (WT) or Res 499 IFNGR KO tumors measured by average expression of *Ki67* and *Top2a*. **E)** Tumor growth of Res 499 IFNGR KO tumors implanted into wild type or FoxP3-DTR mice treated with anti-CTLA4 or diptheria toxin (DT). **F)** Survival of mice bearing CT26 tumors with IFNGR +/− B2M KO after treatment with anti-PD1 or anti-CTLA4. For all groups, n=5. **G)** Top predictive features from a random forest model (and confirmed by lasso regression) for how the proportion of different intratumoral immune cells (x-axis) predicts the proportion of activated NK cells in human melanoma tumors (y-axis). Standard error is in yellow. See also Figure S6.
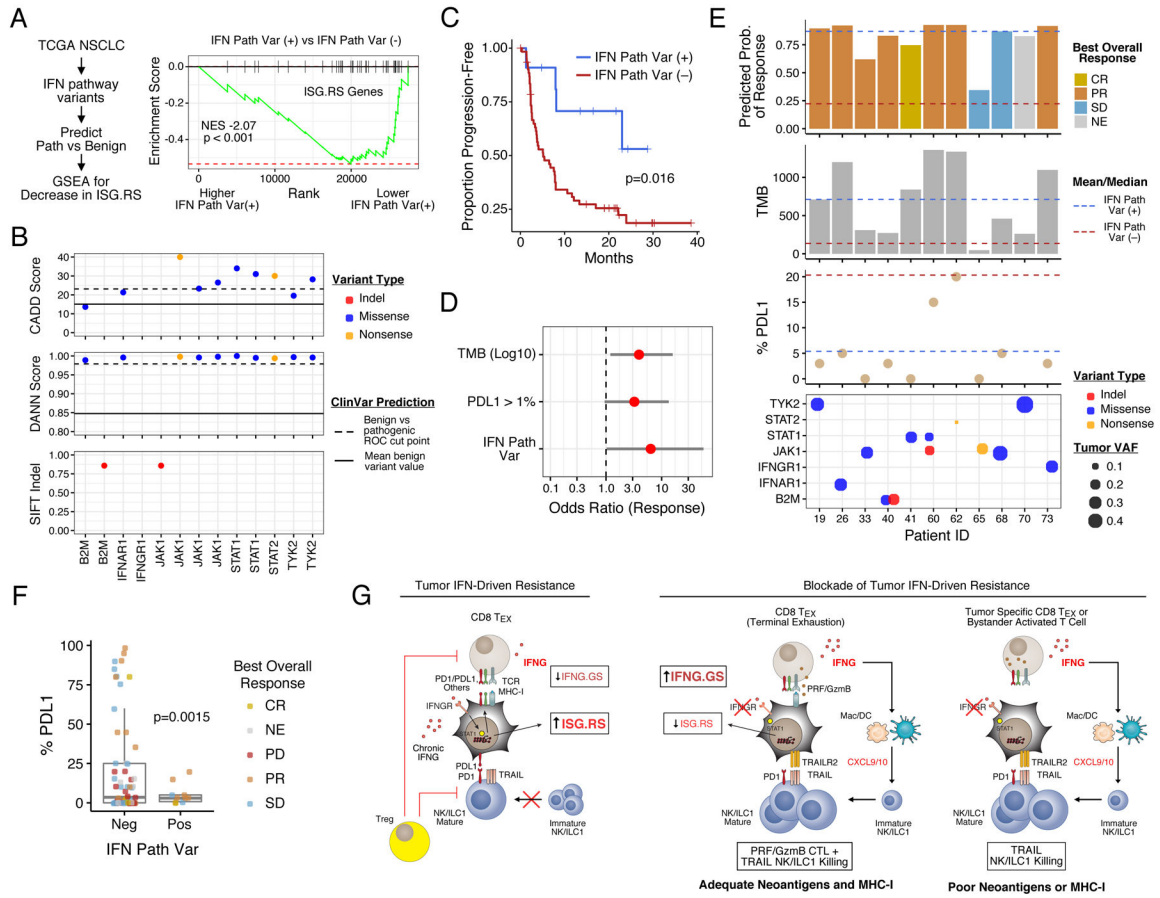
Figure 7. Tumor mutations in the IFN pathway predict decreased ISG.RS and increased survival in lung cancer patients treated with anti-CTLA4 and anti-PD1.
A) GSEA of ISG.RS genes comparing TCGA NSCLC patients with and without a predicted pathogenic variant in the IFN pathway (IFN Path Var). **B)** CADD, DANN, and SIFT scores for IFN Path Var from a cohort of 75 NSCLC patients treated with anti-CTLA4 + anti-PD1. Variant type (color), optimal cut points for classification (dashed line), and mean value for benign ClinVar variants (solid line) are shown. **C)** Progression-free survival after anti-CTLA4 and anti-PD1, and **D)** odds ratios for response (with 95% confidence intervals) from multivariable logistic regression. **E)** Response (top plot), clinical features (middle two plots), and variant allele frequency (VAF; bottom plot) of tumors with IFN Path Vars. The mean/median values are indicated by dashed lines. Top plot shows predicted probability of response (from logistic regression) and observed best overall response (NE is nonevaluable). **F)** Boxplot of %PDL1 staining and response. **G)** Model for how the opposing roles of IFN signaling in immune and tumor cells regulate ICB response in tumors differing in neoantigen and MHC-I status. See also Figure S7.

KEY RESOURCES TABLE

REAGENT or RESOURCE	SOURCE	IDENTIFIER
Antibodies		
Anti-mouse GzmB	Invitrogen	Cat# GRB18
Anti-mouse NKG2A/C/E	BD Pharmagen	Custom (Clone 20d5)
Anti-mouse CD4	BD Biogen	Cat# 565978
Anti-mouse Ki67	BD Biosciences	Cat# 563757
Anti-mouse NKG2D	BD Pharmagen	Custom (Clone CX5)
Anti-mouse KLRG1	BD Pharmagen	Custom (Clone 2F1)
Anti-mouse CD11b	BD Biogen	Cat# 565080
Anti-mouse CD45.2	BD Biogen	Cat# 564880
Anti-mouse NKp46	BD Biogen	Cat# 561169
Anti-mouse CD69	BD Pharmagen	Cat# 557392
Anti-mouse Ly49A	BD Biogen	Custom (Clone A1)
Anti-mouse CD49b	Invitrogen	Cat# 46-5971-81
Anti-mouse TCRB	BD Pharmagen	Custom (Clone H57–597)
Anti-mouse NK1.1	eBioscience	Cat# 47–5941
Anti-mouse CD27	BD Pharmagen	Custom (Clone LG3A.10)
Anti-mouse TRAIL	Biolegend	Cat# 109309
Anti-mouse Eomes	eBioscience	Cat# 50–4875
Anti-mouse TIGIT	BD Biosciences	Cat# 565270
Anti-mouse Lag3	Biolegend	Cat# 125219
Anti-mouse CD127	Biolegend	Cat# 135025
Anti-mouse Tbet	BD Biogen	Cat# 564142
Anti-mouse Ly49D	BD Biogen	Cat# 742559
Anti-mouse CD44	Biolegend	Cat# 103031
Anti-mouse CTLA4	Biolegend	Cat# 106306
Anti-mouse CD8a	MBL International	Cat# T03015
Anti-mouse PD1	Biolegend	Cat# 109110
Anti-mouse CD3	Biolegend	Cat# 107631
Anti-mouse CD49a	Biolegend	Cat# 142604
Live/Dead Aqua	Life Technologies	Cat# L34957
Anti-mouse PD-L1	eBioscience	Cat# 46–5982
Anti-mouse TRAILR2	Biolegend	Cat# 119905
Anti-human CD19	Biolegend	Cat# 302211
Anti-mouse H2-Kb/Db	Biolegend	Cat# 114612
Anti-mouse CTLA4 (9H10)	BioXcell	Cat# BE-0131
Anti-mouse CTLA4 (9D9)	BioXcell	Cat# BE0164
Anti-mouse PD1	BioXcell	Cat# BE0146

REAGENT or RESOURCE	SOURCE	IDENTIFIER
Anti-mouse CD8a	BioXcell	Cat# BE0061
Anti-mouse NK1.1	BioXcell	Cat# BE0036
Anti-mouse asialo-GM1	Wako Chemical	Cat# 986–10001
Anti-mouse IFNg	Biolegend	Cat# 505821
Bacterial and Virus Strains		
Biological Samples		
Chemicals, Peptides, and Recombinant Proteins		
IFNG	Peprotech	Cat# 315–05
Ova Peptide	Invivogen	Cat# sin-vac
CXCL10	Peprotech	Cat# 250–16
Poly I:C	Invivogen	Cat# vac-pic
Critical Commercial Assays		
LegendPlex Cytokine Assay	Biolegend	Cat# 740005
Purelink Genomic DNA Kit	ThermoFisher Scientific	Cat# K182001
SureSelectQXT Kit	Agilent	Cat# G9683A
10x v2 Library and Gel Bead Kit	10x Genomics	Cat# PN-120258
Fixation and Permeablization Kit	eBioscience	Cat# 00–5523
Deposited Data		
499 WT v 499 IFNgR KO s.c. RNA-seq data	GSE131927	
B16 v 499 Whole Exome Seq	GSE131927	
Sorted 499 tumor cells	GSE83848	
Experimental Models: Cell Lines		
B16-F10 melanoma	ATCC	Cat# CRL-6475
TSA breast carcinoma	Laboratory of Sandra Demaria	PMID: 19706802
CT26 colorectal carcinoma	ATCC	Cat# CRL-2638
Res 499, Res 237, associated CRISPR KO	Laboratory of Andy Minn	PMID:25754329, PMID:27912061
Experimental Models: Organisms/Strains		
C57BL/6 WT mice	Jackson Laboratories	Cat# 000664
C57BL/6 WT mice	Charles River Laboratories	Stock #027
Balb/c WT mice	Charles River Laboratories	Stock #028
RAG$^{-/-}$ mice (B6129S7-Rag1^{tm1Mom}/J)	Jackson Laboratories	Cat# 002216
IFNg $^{-/-}$ mice (C57BL/6-Tg(TcraTcrb)1100Mjb/J)	Jackson Laboratories	Cat# 002216
FoxP3 DTR mice (B6.129(Cg)-FoxP3$^{tm3(DTR/GFP)Ayr}$/J)	Jackson Laboratories	Cat# 016958
OT-I mice (C57BL/6-Tg(TcraTcrb)1100Mjb/J)	Jackson Laboratories	Cat# 003831
Oligonucleotides		

REAGENT or RESOURCE	SOURCE	IDENTIFIER
B2M guide sequence g1: GACAAGCACCAGAAAGACCA g2: GTGAGTATACTTGAATTTGA	This paper	
TRAILR2 guide sequence g1: GTGGGCGTGCTGGGTCCTGG g2: ATCGTCCAGCTGGCCTACAG	This paper	
Recombinant DNA		
Human-CD19 expression vector	Laboratory of Carl June	PMID:19384291
Anti-human CD19BBz CAR construct	Laboratory of Carl June	PMID:26885860
Software and Algorithms		
Picard tools v2.17.11	https://broadinstitute.github.io/picard/	
samtools v1.3.1	http://samtools.sourceforge.net	
survival v2.41–3	https://cran.r-project.org/web/packages/survival/index.html	
MASS v7.3–48	https://cran.r-project.org/web/packages/MASS/index.html	
DESeq2 v1.14.1	https://bioconductor.org/packages/release/bioc/html/DESeq2.html)	
fgsea v1.4.1	https://bioconductor.org/packages/release/bioc/html/fgsea.html	
SAVER v1.1.1	https://github.com/mohuangx/SAVER	
Rtsne v0.15	https://github.com/jkrijthe/Rtsne	
CIBERSORT	https://cibersort.stanford.edu/	
randomForestSRC v2.5.1.14	https://github.com/kogalur/randomForestSRC	
flowCore v1.44.1	https://bioconductor.org/packages/release/bioc/html/flowCore.html	
cytofkit v1.10.0	https://bioconductor.org/packages/release/bioc/html/cytofkit.html	
fastQC v0.11.5	https://www.bioinformatics.babraham.ac.uk/projects/fastqc/	
GATK v4.0.2.1	https://software.broadinstitute.org/gatk/gatk4	
bwa v0.7.17	http://bio-bwa.sourceforge.net/	
Canopy v1.3.0	https://github.com/yuchaojiang/Canopy	
NetMHC v4.0	http://tools.iedb.org/main/tcell/	
ANNOVAR	http://annovar.openbioinformatics.org/en/latest/user-guide/download/	
SIFT	http://sift.bii.a-star.edu.sg/www/SIFT_indels2.html)	
Seurat v2.3.4	https://satijalab.org/seurat/install.html	
Cell Ranger v2.1.0	https://support.10xgenomics.com/single-cell-gene-expression/software	
Other		
Diptheria Toxin	Sigma Aldrich	D0564